Technische Universität München
Fakultät für Physik

Abschlussarbeit im Bachelorstudiengang Physik

dE/dx studies with π and e tracks of the ALICE GEM IROC prototype

dE/dx Untersuchungen mit π und e Spuren am ALICE GEM IROC Prototypen

Paul Philipp Gadow

Monday 26th August, 2013

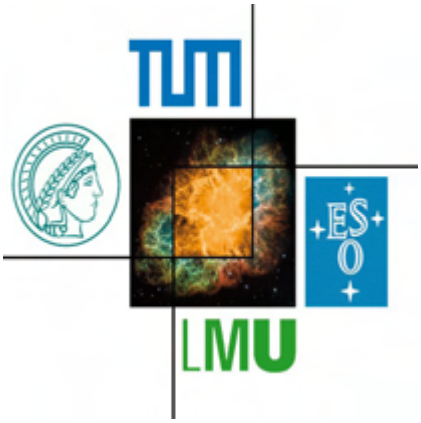

Erstgutachter (Themensteller): Prof. L. Fabbietti
Zweitgutachter: Prof. L. Oberauer

Betreuer: Sverre Dørheim

Bachelor-Kolloquium: 27.08.2013

Abstract

A time projection chamber (TPC) is a large volume tracking detector measuring coordinates in space and specific energy loss along trajectories of charged particles, even in high-multiplicity events. TPCs have been successfully used in several experiments including ALICE at CERN. The charge amplification is conventionally accomplished by multi-wire proportional chambers (MWPCs), which require gating grids to prevent ions from drifting back into the drift volume and from distorting the drift field, thus limiting the trigger rate to $\mathcal{O}(1\,\mathrm{kHz})$. The use of Gas Electron Multiplier (GEM) for gas amplification in TPCs has been introduced as an alternative and was successfully implemented in the FOPI experiment at FAIR, Darmstadt [10]. The GEM's intrinsic ion-backflow suppression presents an oppurtunity to run the detector without gating, allowing higher trigger rates as have been already achieved at the LHC after the upgrade.

This thesis investigates the charged-particle identification capabilities of an Inner Readout Chamber (IROC) prototype of the ALICE TPC equipped with a stack of three GEMs by the means of specific energy loss (dE/dx) measurements. The prototype has been tested at the T10 beam line at Proton Synchrotron (PS) at CERN, using beams consisting predominantly of electrons and pions at momenta of 1 GeV/c up to 6 GeV/c, varied over different runs. Energy loss spectra are obtained from reconstructed particle tracks by the method of the truncated mean. From the spectra the relative energy resolutions are extracted and used to extract the separation power between pions and electrons at fixed momenta The energy resolution of the ALICE IROC prototype for different HV settings was in the interval 9 % to 11 % for electrons and in the interval 11 % to 14 % for pions at a beam momentum of 1 GeV/c The results for the separation power between electrons and pions were spread around 4 σ for a beam momentum of 1 GeV/c and around 3 σ for a beam momentum of 2 GeV/c. The obtained values for electrons at 1 GeV and the separation power agree with a previous analysis of the data by Jens Wiechula and Martin Ljunggren [36].

Contents

Chapter 1

Introduction

1.1 The ALICE Experiment

The ALICE detector [5], shown in figure 1.1, investigates collision of heavy lead ions (^{82}Pb). In 2010 and 2011 ALICE was operated at a center of mass (cms) energy of $\sqrt{s} = 2.76$ TeV/nucleon with an integrated luminosity of $L_{\text{int}} = 0.16\,\text{nb}^{-1}$ [36]. The collisions happen in the radial center of the detector. In these collisions a fireball of very high temperature can form due to the high center of mass energy, where a quark-gluon-plasma is created, in which the constituents of the nuclei - quarks and gluons - behave as free particles. The plasma expands adiabatically and cools to a temperature of $2 \times 10^{12}\,\text{K}$, where quarks und gluons recombine to hadronic matter. The mesons and baryons created in this hadronization process exit the fireball and can be measured in the detectors. A challenge for the detectors is the high track multiplicity. In simulations of Pb-Pb-collisions up to 20 000 tracks in the TPC were predicted [5]. By measuring the collision temperature and the distribution of the created hadrons and comparing them to those of plasma free proton-proton collisions conclusions on the quark-gluon-plasma's properties can be made.

1.1.1 Physics campaign in the ALICE experiment

The long-term goal of ALICE is the precise characterization of the quark-gluon-plasma [31]. The quark-gluon-plasma is assumed to be the state of matter which predominantely existed in the first picoseconds to 10 microseconds of the electro-weak phase transition in the big bang model. By determination of its properties, including critical temperature, degrees of freedom, speed of sound and transport coefficients, a better understanding of quantum chromodynamics as a multi-particle theory can be achieved. Experiments like ALICE contribute towards the characterization of strongly interacting matter at high temperatures by studying rare probes, their collective properties and their hadronization.

1.1.2 Upgrade Strategy for ALICE at High Rate

To investigate the questions concerned with the quark gluon plasma, the experimental approach taken by ALICE is to increase the collision frequency of 8 kHz to 50 kHz for lead collisions and to increase the integrated luminosity to $L_{\text{int}} = 10\,\text{nb}^{-1}$ [31]. To run a near minimum bias mode, the Inner Tracking System will be rebuilt and the ALICE detectors will be modified to provide a fully pipelined readout, implying a major upgrade of the data acquisition and trigger system to build on ALICE's capabilities of excellent tracking in a most high multiplicity environment and particle identification over a large range of transverse momenta. The operation of the TPC at a rate of 50 kHz cannot be accomplished with an active ion gating scheme as it has been used until now to prevent the backflow of ions in the drift region of the TPC and therefore prevent distortions of the drift field. With the current setup the TPC cannot be triggered at rates exceeding 3.5 kHz [31]. Therefore the replacement of the existing MWPC-based readout chambers by a multiple-stage GEM stack was proposed. GEMs have proven their reliability in high-rate applications, provide intrinsic supression of ion-backflow and allow the TPC to operate continuously in an ungated readout mode.

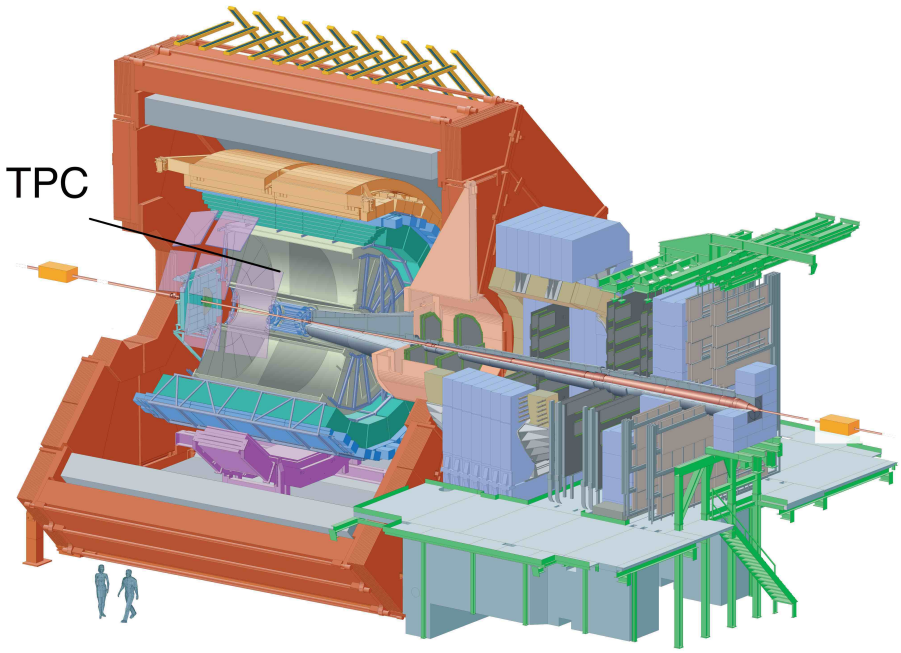

Figure 1.1: Artistic view of the ALICE detector indicating the position of the TPC [5]

1.2 The ALICE-Time Projection Chamber

A Time Projection Chamber (TPC) [32] is an advanced particle detector, which has been successfully used in various particle physics experiments such as PEP-4 [3], ALEPH [9], DELPHI [18], NA49 [2], FOPI [16], STAR [8] [1] and ALICE [5]. Usually a TPC consists of a large cylindrical volume centered around the interaction vertex, which is inside of a solenoid magnetic field and filled with gas. The TPC is the main component of the ALICE detector and is able to determine tracks, measure the particle's momentum, determine vertices and identify particles by analyzing the particle's energy loss. A TPC makes use of ideas from MWPC detectors and drift chambers and is essentially a large gas-filled cylinder [28]. Due to its size the ALICE TPC is separated in two parts by a high voltage electrode at the center. A uniform electric field along the beam axis is created by the application of voltage between the endcaps of the cylinder and the electrode. A magnetic field parallel to the beam is applied for measuring the particles momentum and to reduce the transverse diffusion of drifting particles in addition. Since the electric field has to be highly homogenous to obtain a good spatial resolution, a so-called "field cage" consisting of a series of field strips surrounds the cylindrical volume and divides the potential from the cathode stepwise down to the anode, so that distortions of the drift field are minimized.

The active volume of the ALICE-TPC is $88\,\mathrm{m}^3$ and consists of a cylinder which spans 500 cm along the beam pipe and extends from 85 cm to 250 cm in radial dimension [5]. The cylindrical field cage is filled with a Ne/CO_2 (90/10) gas mixture with 100 ppm H_2O, less than 1 ppm O_2 and less than 10 ppm of other gases, but also other gas mixtures were tested [36]. In the center of the chamber one can find the drift electrode, which is held at a potential of 100 kV. The end plates consist of 18 sectors each covering 20° in azimuthal angle, where multiwire proportional chambers (MWPCs) are seated on top of cathode readout pads. They are shown in figure 1.2 together with the coordinate systems of ALICE. The trapezoidal detector elements in radial distance of 84.4 cm to 132 cm to the center of the cylinder are called Inner Readout Chambers (IROC), whereas the detector elements in radial distance of 134.6 cm to 246.6 cm are called Outer Readout Chambers (OROC). The detector covers almost a full solid angle of 4π. The ALICE TPC's spatial resolution is 300 µm and its dE/dx-resolution is $5-7\%$. The potential applied to the drift cathode results in a constant drift field of 400 V/cm throughout the detector volume [22]. Using the gas mixture of Ne/CO_2 (90/10) the maximum drift time is 88 µs . The MWPCs provide a gain of around 7×10^3 [5].

1.2.1 Principles of Operation of the ALICE GEM-TPC

While in the traditional TPC the ends of the cylinder are covered by a sector array of proportional anode wires to cause gas amplification of the primary ionization

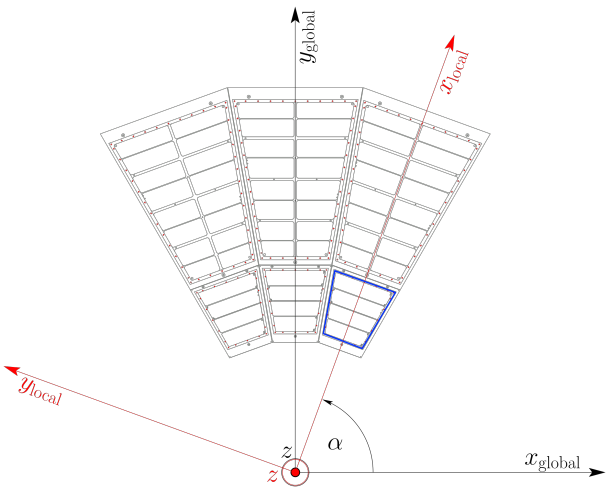

Figure 1.2: IROCs (*blue*) and OROCs on an endcap, shown together with the ALICE coordinate systems.

charge carriers, in the ALICE GEM-TPC GEMs take the role of the anode wires. After the gas amplification the charge carriers induce a signal on the readout pads behind the amplification stage. In contrast to MWPCs, electrons instead of ions induce the signal in a GEM-TPC, resulting in a much faster signal with different polarity, which is of advantage in a high multiplicity environment to prevent pileup. As the cylinder is centered on the interaction point of a collider, particles emanating from this point pass through the gas filled chamber, ionize the gas molecules and produce ions and free electrons, which drift towards the endcaps (in case of the ions to the drift electrode). This process is illustrated in figure 1.3. When the electrons reach the end caps, they are accelerated by the electric field of the anode wires of the MWPC and produce an electron avalanche by ionizing additional gas molecules during the acceleration. The coordinate, where the primary electron was created by the ionizing particle, can be calculated from the signals induced on a plane of cathode pads below the anode wires. The projection of the space point on the pad plane is given by the center of gravity of the amount of charge induced on the pads. The third coordinate along the cylinder axis is given by the drift time of the electrons produced by the ionizing particle. While operating a MWPC TPC, space charge accumulates in the drift volume due to positive ions drifting back towards the central cathode and distorts the drift field. In MWPC TPCs this is prevented by placing a gating grid just before the anode wires, so positive ions are captured at this grid and inhibited from entering the drift volume. In high multiplicity experiments with high trigger rates however, a gating grid cannot be used, since the gating only works for trigger

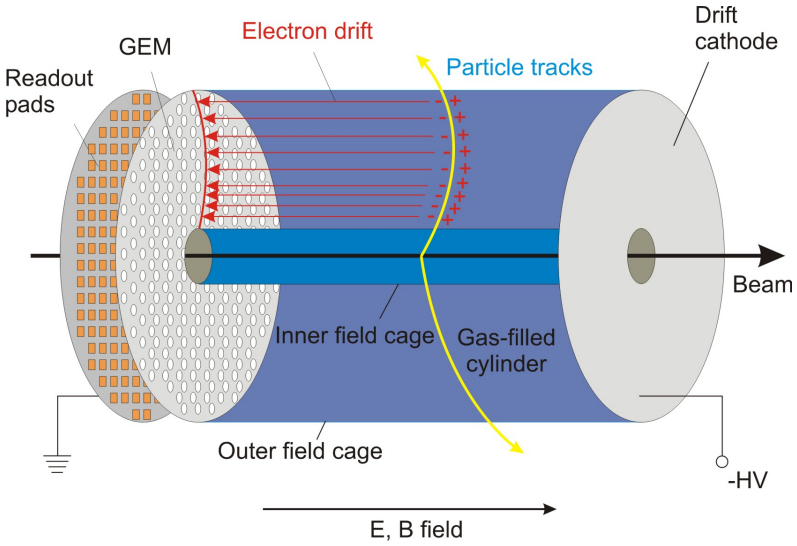

Figure 1.3: Schematic figure of a GEM-based TPC [17]

rates up to $\mathcal{O}(1\,\mathrm{kHz})$. GEMs with their intrinsic ion-backflow supression present a possible choice to overcome the necessity of a gating grid in a TPC.

1.2.2 Gas electron multipliers for gas amplification

F. Sauli presented GEMs as a possible device for charge multiplication [35]. GEMs are a composite grid of two metal layers separated by a thin insulator.

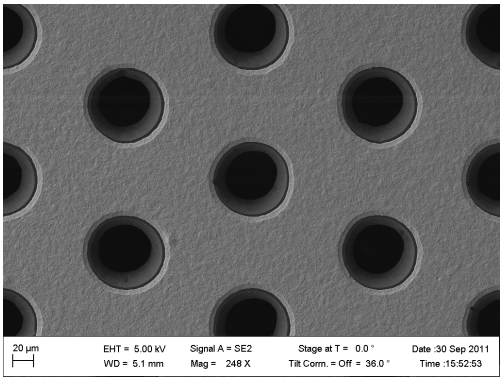

Figure 1.4: Close up view of a GEM under an electron microscope [36]

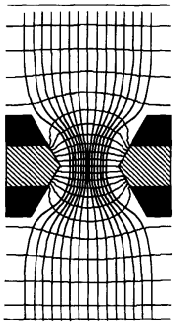

Figure 1.5: Computed electric field in the multiplying hole [35]

Typically, a GEM consists of a 50 µm thin Kapton foil clad with a 5 µm thin layer of copper on both sides, etched with a regular matrix of open channels in a photolithographic process. In this way a dense (10^4 holes/cm^2), regular pattern of holes is formed, which can be seen in figure 1.4.

Due to the etching process, the holes have a double conical shape with an inner diameter of 50 µm, an outer diameter of 70 µm and a pitch of 140 µm. A GEM foil with the electrodes kept at a suitable potential difference (typically 200 - 400 V) can amplify the charge drifting through the holes by multiplication of the electrons [36]. Since the field lines are focused in the holes, as can be seen in figure 1.5, the resulting fields in the GEM holes are very high ($\mathcal{O}(50\,\mathrm{kV/cm})$), so the electrons are accelerated in the holes and ionize gas atoms. The created electrons and ions are accelerated as well, thus creating an avalanche. Multiple GEM foils assembled in a stack in the same gas volume allow even larger effective amplification factors in a succession of steps. The electrons created in a hole are extracted to the next amplification stage, whereas the ions follow the field lines either on the cathode-side of a GEM foil, where they recombine, or go back to the drift volume of the detector. The process of avalanche formation and the principle of ion-backflow are depicted in figure 1.6.

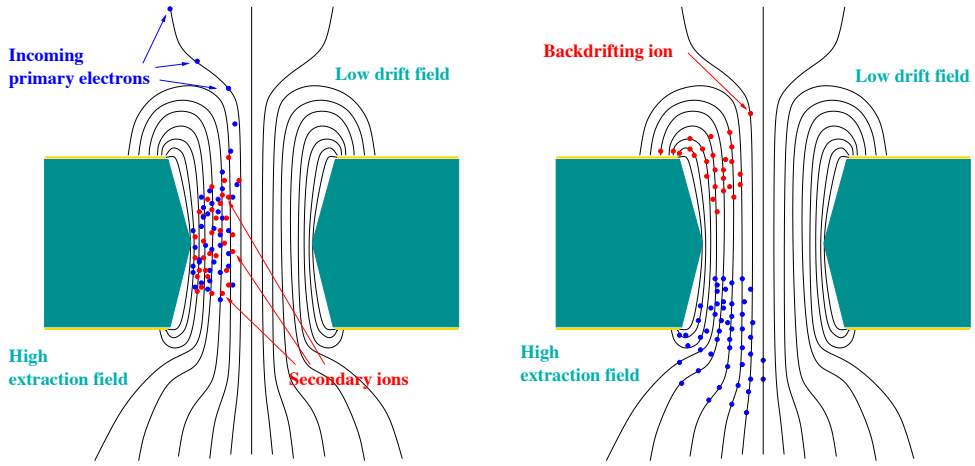

Figure 1.6: Working principle of a GEM: a) Incoming primary electrons follow the field lines of the low drift field into the hole, where the acceleration of the high electric field causes avalanche multiplication of electron-ion pairs. b) The small mobility of the ions together with an asymmetric field configuration prevent the backflow of ions in the drift volume [17].

GEMs have been successfully employed in GEM-based tracking detectors, used in the COMPASS experiment at CERN [26]. GEMs have been successfully used for gas amplifiction in the FOPI TPC [10], in LHCb [20] and TOTEM [37].

1.3 Analysis of the data sample by University of Tübingen

An analysis of the data sample was done by Jens Wiechula, University of Tübingen, and Martin Ljunggren, Lund University, in order to evaluate the dE/dx measurement capabilities of the IROC prototype [36]. The methods used and the results shall be reviewed and briefly discussed.

The data obtained by means discussed in chapter 3 consisted of signals with amplitude, time and pad ID. Only samples within a time interval 1 µs to 4 µs were accepted. Gain equalization was realized by using the electron tracks and normalizing the maximum charge for each pad to the median, thus producing a gain map for each run. The maps for all runs were averaged resulting in a map used for gain corrections. Because sector gaps were still visible in the gain map, the rows 9, 17, 25, 32, 39, 45, 51 and 57 of the readout pad were excluded from the analysis. Since the front-end cables of the first two pad rows were mapped wrong, the gain correction algorithm was only sufficient for 46 pad rows to which the analysis was confined. A simple clustering was applied on the signals by looking for local maxima of the amplitude on pads and combining the pad with the maximum amplitude in the center with the 8 adjacent pads (or less in corners) and if those also had a signal with their neighbours to a cluster. To be considered a local maximum, the amplitude of the pad had to exceed 4 ADC counts and in addition 2 samples above the threshold were required. The position of the cluster was obtained by a center of gravity method by calculating the amplitude weighted average in pad and time direction.

A track finder combined the clusters to tracks. A track is supposed to have at least 10 clusters and can have up to 3 gaps between clusters. The track finder starts with the cluster in the last pad row and associates clusters of the next row to a track, using a search road of 3 pads and 3 time bins. The track finder is iterated until all clusters are processed, then two linear fits are applied to the clusters associated to a track, one in pad and row, the other one in time and row.

For the dE/dx measurements only single-track events were accepted, with an additional cut on the number of clusters in a track $n > 32$ (except for a gain scaling of 100 and the transfer field $2 < 400\,\mathrm{V/cm}$). In order to distinguish between electron and pion tracks, electrons were selected using the signal of a Čherenkov counter, which had to exceed a threshold of 400, respectively events below a treshold of 150 were regarded as pions. To symmetrize the energy loss distributions, a truncated mean method was used, which selected the interval of $5 - 75\%$ of the samples. With gain

correction about 0.5% better resolution was achieved. No corrections for pressure and temperature variations were applied.

The results of the analysis for different setups, which are discussed in chapter 3, are shown in figures 1.8 and 1.7. The seperation power defined in chapter 2 provides a measure for the particle identification capabilities of a detector, which is better for lower beam momenta and higher gas amplification. In Monte Carlo simulations of a dE/dx spectrum for 1 GeV/c pions using information from all 63 rows of the padplane resulted in a relative resolution of 9.0% [36]. The measured resolutions for electrons move between 9 % to 11 %, whereas the measured resolutions for pions move between 10 % to 12 %. The disagreement with the simulation results from the reduced number of rows used in the analysis.

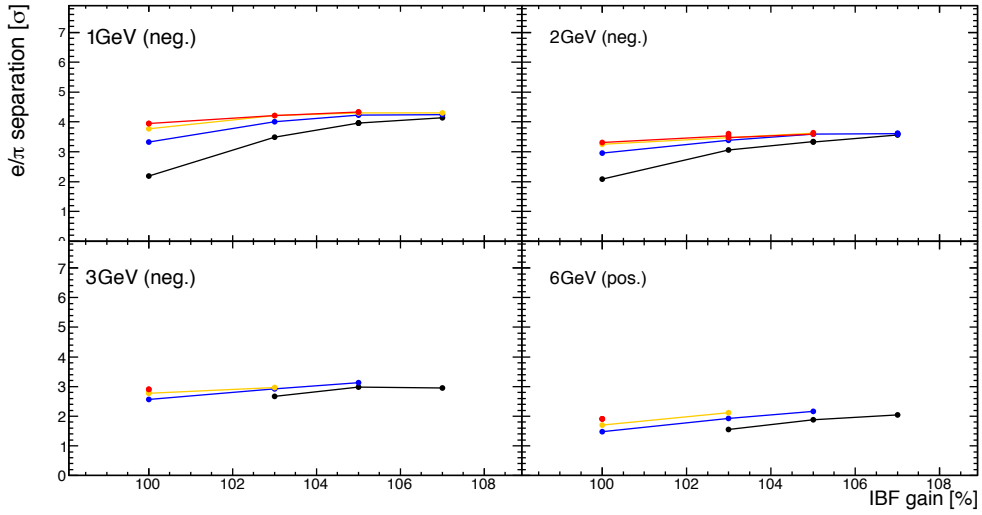

Figure 1.7: Separation power between pions end electrons with 1 GeV/c to 6 GeV/c momentum measured for different HV settings [36].

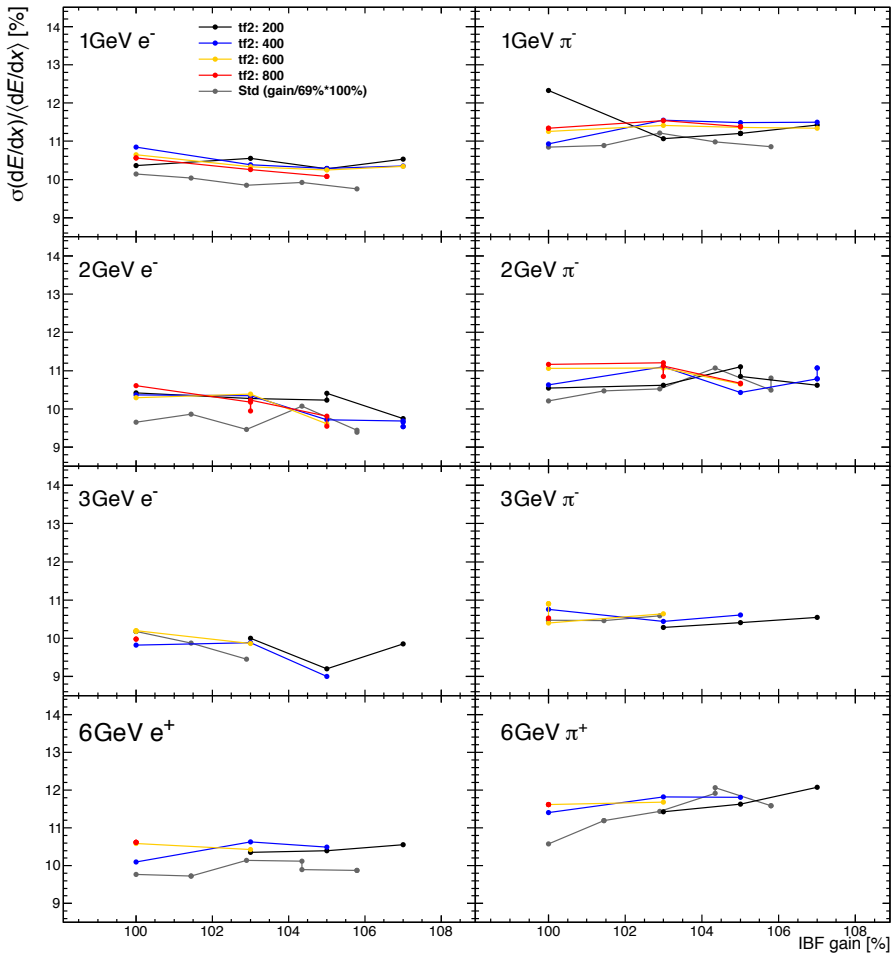

Figure 1.8: The relative dE/dx resolution measured for different HV settings for electrons and pions with momentum ranging from 1 GeV/ c to 6 GeV/ c by the Tübingen dE/dx analysis [36].

Chapter 2

Foundations

2.1 Particle identification

Particle identification (PID) is fundamental to particle physics experiments [29]. Some strategies and methods used in the analysis of the GEM IROC test run at the PS will be briefly discussed. Measuring a particle's momentum and velocity simultaneously allows determination of its mass, since the momentum of a relativistic particle is given by $\boldsymbol{p} = mc\boldsymbol{\beta}\gamma$ and its velocity by $\boldsymbol{v} = c\boldsymbol{\beta}$, so its mass can be obtained by means of

$$m = \frac{p}{c\beta\gamma}. \tag{2.1}$$

The mass resolution is given by

$$\left(\frac{dm}{m}\right)^2 = \left(\frac{dp}{p}\right)^2 + \left(\gamma^2 \frac{d\beta}{\beta}\right)^2. \tag{2.2}$$

The particle's momentum can be determined by its curvature in a magnetic field, while its velocity can be obtained by measurements of its emitted Čherenkov radiation, energy loss due to ionization (dE/dx), Time of Flight (TOF) and emission of transition radiation, the latter two not being discussed in this context. In addition to PID by mass determination, information can be obtained by the characteristic signatures particles leave in the detector caused by particle families' different interactions with matter.

2.1.1 Energy resolution and separation power

The energy registered in a detector is subject to fluctuations. For instance, radiation quanta of a single fixed energy will be spread out over more than just one channel in the detector. The energy resolution is a measure for the capability of a detector to distinguish between two peaks in an energy spectrum. For a Gaussian distribution describing the energy deposit in the detector with mean μ and standard deviation

σ, the relative energy resolution is defined as

$$\text{rel. res.} = \frac{\sigma(dE/dx)}{\langle dE/dx \rangle}. \tag{2.3}$$

The separation power for two particles A and B with the same momentum, but different masses is defined as

$$n_{\sigma_E} = \frac{\mu_A - \mu_B}{(\sigma_E^A + \sigma_E^B)/2}. \tag{2.4}$$

2.2 Energy loss of charged particles in matter

When a particle passes through matter, it loses part of its kinetic energy due to inelastic Coulomb collisions with atomic electrons of the material. The atoms of the material are excited or even ionized, if the energy transfer exceeds the ionization energy of the particular atom. The average energy loss per unit path length $\langle dE/dx \rangle$ cannot be measured directly, however assuming a linear correlation between the ionization of the medium and the energy loss of the particle, it can be measured in terms of the average number of electron/ion pairs $\langle n \rangle$, that are produced while the particle passes through a medium of length x, provided the average energy W spent for the creation of one electron-ion pair is known:

$$\left\langle \frac{dE}{dx} \right\rangle = \frac{\langle n \rangle W}{x}. \tag{2.5}$$

Typical values of W for relativistic particles passing through a gas lie around 30 eV and can be assumed as constant factors [33]. The total energy loss of a heavy, charged particle with respect to a given differential cross section $d\sigma(E)/dE$ is given by

$$\frac{dE}{dx} = N \int_0^{E_{\max}} E' \frac{d\sigma}{dE'} dE', \tag{2.6}$$

where N denotes the volume density of electrons in the traversed region.

The mean energy loss per unit length of a particle passing through matter was derived in a perturbative calculation by Bethe [12], assuming energy transfer by soft and hard collisions. It extends only to energies, above which atomic effects are not important. The mean energy loss of a moderately relativistic particle can be described by

$$\left\langle -\frac{dE}{dx} \right\rangle = \frac{4\pi}{(4\pi\varepsilon_0)^2} \frac{z^2 e^4 N}{mc^2\beta^2} \left[\frac{1}{2} \ln \frac{2mc^2\beta^2\gamma^2 T_{\max}}{I^2} - \beta^2 - \frac{\delta}{2} \right], \tag{2.7}$$

with ze the charge of the particle, N the electron density of the medium, m the electron mass, $T_{\max}$ the maximum kinetic energy transmitted in a collision to an atomic electron, I mean excitation energy of the medium and δ the density effect correction. The stopping power $\langle dE/dx \rangle$ for positive muons in copper is shown in figure 2.1.

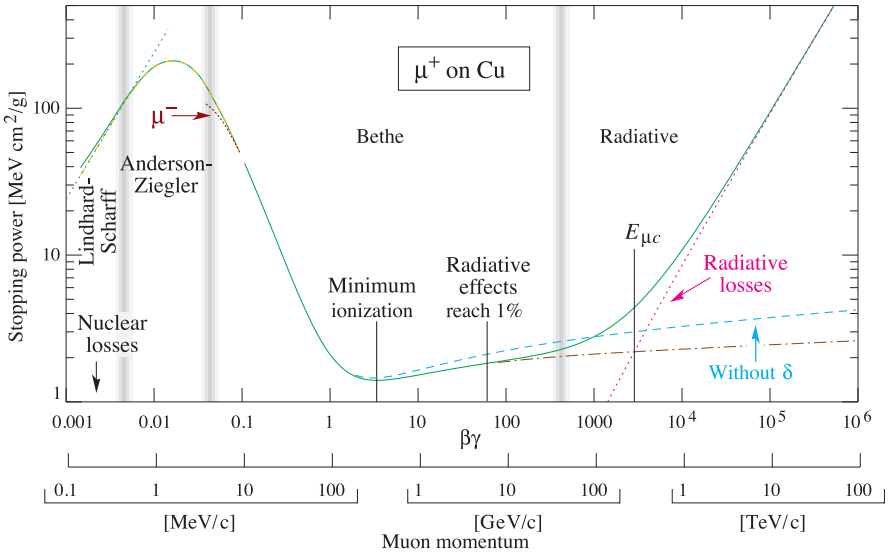

Figure 2.1: Stopping power for positive muons in copper. Solid curves indicate the total stopping power, vertical bands indicate boundaries between different approximations made to calculate the stopping power [11].

It should be noted that equation (2.7) does not depend on the particle's mass, however, at fixed momentum $p = \beta\gamma mc = \text{const}$, $\beta\gamma$ depends on m. For the energy loss E per traveled distance x measured with sufficiently precise resolution, this allows the separation of different particles with the same measured momentum.

2.2.1 Distribution of a charged particle's energy loss

Since the energy loss of a charged particle is a statistical process, the distribution $F(x, \Delta)$ of the energy loss Δ per length x of the particle's path through the medium, commonly known as 'straggling function', is of great interest. The two most prominent methods to determine it are the Laplace transformation method [27] and the convolution method [14].

Typical for energy loss distributions is their assymetric shape, which is shown in figure 2.2. The long tail towards high energy deposits comes from single collisions

with large energy transfer. Therefore one can not simply calculate the mean of the distribution to obtain the most probable value, but has to apply for instance the method of the truncated mean, where only a certain percentage of the energy loss samples is evaluated in calculating the mean.

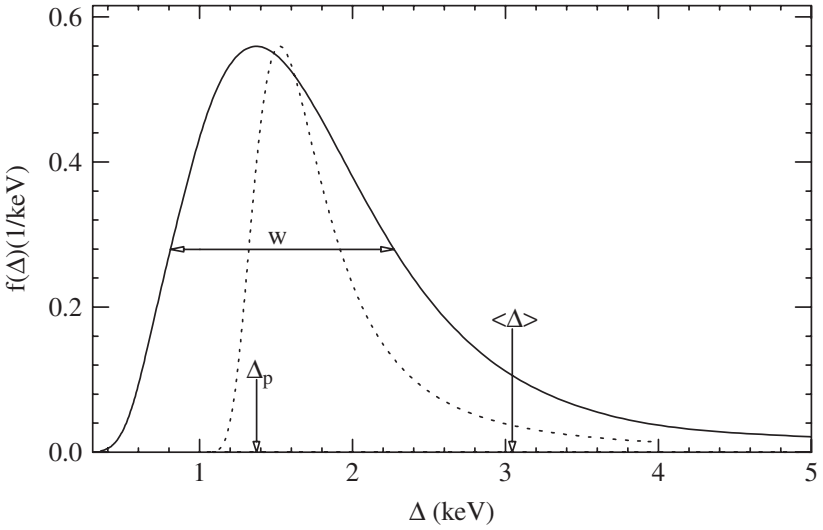

Figure 2.2: Straggling function $F(x, \Delta)$ for particles traversing 1.2 cm Ar gas with $\beta\gamma = 3.6$ as obtained with the PAI model (solid line). The original Landau function is represented by the dotted line. The most probable energy loss Δ_p, the mean energy loss Δ and the full-width-half-maximum W are shown as describing parameters of the distribution [13].

Both calculations of the energy loss distribution are determined by the electron density N and the cross section $d\sigma/dE$. The question remaining is how to model this cross section. Quantum mechanical models describing even shell excitations exist, the most common is the Photo Absorption Ionization (PAI) model [6].

2.2.2 Photo Absorption Ionization model (PAI)

Considering fast charged particles losing their energy in a number of independent soft collisions with the medium's bound electrons in a semiclassical treatment, Allison and Cobb (1980) [6] derive the mean energy loss per unit length due to the longitudinal

component of the electric field of the fast moving, charged particle

$$\left\langle \frac{dE}{dx} \right\rangle = -\int_0^\infty d\omega \, \frac{e^2}{\beta^2 c^2 \pi} \left[\frac{Nc}{Z} \sigma_\gamma(\omega) \ln[(1-\beta^2\varepsilon_1)^2 + \beta^4\varepsilon_2^2]^{1/2} \right. \tag{2.8}$$

$$+ \omega \left(\beta^2 - \frac{\varepsilon_1}{|\varepsilon|^2} \right) \arg\left(1 - \varepsilon_1\beta^2 + i\varepsilon_2\beta^2\right) \tag{2.9}$$

$$\left. + \frac{Nc}{Z} \sigma_\gamma(\omega) \ln\left(\frac{2m\beta^2c^2}{\hbar\omega} \right) + \frac{1}{\omega} \int_0^\omega \frac{\sigma_\gamma(\omega')}{Z} d\omega' \right], \tag{2.10}$$

with the medium's dielectric constant $\varepsilon = \varepsilon_1 + i\varepsilon_2$ expressed in terms of the generalized oscillator strength, the energy transfer $\hbar\omega$ and the photoabsorption cross section $\sigma_\gamma = Z\omega\varepsilon_2/Nc\sqrt{\varepsilon_1}$. Where the expression for the mean energy loss in 2.7 is derived in a perturbative calculation, in the PAI model it is derived from the electric field at the position of the charged particle and the energy loss is described as the effect of this electric field doing work on the particle. Interpreting equation in terms of the number of discrete collisions with energy transfer $\hbar\omega$ and comparing with

$$\left\langle \frac{dE}{dx} \right\rangle = -\int_0^\infty NE \frac{d\sigma}{dE} \hbar d\omega, \tag{2.11}$$

one obtains the desired differential cross section as predicted by the PAI model

$$\frac{d\sigma}{dE} = \frac{\alpha}{\beta^2\pi} \frac{\sigma_\gamma(E)}{EZ} \ln\left[(1-\beta^2\varepsilon_1)^2 + \beta^4\varepsilon_2^2\right]^{-1/2} \tag{2.12}$$

$$+ \frac{\alpha}{\beta^2\pi} \frac{1}{N\hbar c} \left(\beta^2 - \frac{\varepsilon_1}{|\varepsilon|^2} \right) \arg\left(1 - \varepsilon_1\beta^2 + i\varepsilon_2\beta^2\right) \tag{2.13}$$

$$+ \frac{\alpha}{\beta^2\pi} \frac{\sigma_\gamma(E)}{EZ} \ln\left(\frac{2mc^2\beta^2}{E} \right) + \frac{\alpha}{\beta^2\pi} \frac{1}{E^2} \int_0^E \frac{\sigma_\gamma(E')}{Z} \, dE. \tag{2.14}$$

The first and the third term describe the energy loss by ionization, whereas the second term describes the energy loss by radiation. The last term describes the energy loss by ionization, for high energy transfers it becomes the dominant term and approaches the Rutherford cross section. The PAI model predicts a specific energy resolution in terms of FWHM[1] (%) for argon of

$$R(n, \Delta x, P) = 96 \cdot n^{-0.43} (\Delta x P)^{-0.32}, \tag{2.15}$$

[1] full width half maximum

where n denotes the number of dE/dx samples, Δx the sample size in cm and P the pressure in atm. The exponent -0.43 was chosen instead of the original -0.46, which was calculated for a maximum likelihood analysis, to represent the truncated mean analysis which was applied in this analysis [38].

The prediction for argon in equation (2.15) can be extrapolated for a Ne/CO_2 (90/10) gas mixture with ionization potential I and mean number of electrons per molecule ν by multiplication with the factor $\left(\frac{\nu/I}{\nu_{Ar}/I_{Ar}}\right)^{-0.32}$. With the parameters listed in table 2.1, one obtains the factor 1.28. Assuming a Gaussian distribution, the relative resolution of distribution is rel. res. $= (8 \cdot \ln 2)^{-0.5} \cdot R(n, \Delta x, P)$.

The relative resolution predicted by the PAI model for Ne/CO_2 (90/10) is

$$\text{rel. res. } (n, \Delta x, P) = 52 \cdot n^{-0.43} (\Delta x \cdot P)^{-0.32}. \tag{2.16}$$

Table 2.1: Ionization potentials and number of electrons/molecule for Ar and Ne/CO_2 (90/10)

mean ionization energy Ar	I_{Ar}	26.4 eV [15]
number of electrons/atom Ar	ν_{Ar}	18
mean ionization energy Ne/CO_2	I	35.2 eV [17]
mean number of electrons/molecule Ne/CO_2	ν	11.2

2.2.3 Čherenkov detectors

With the emission of Čherenkov radiation, a threshold velocity of a particle can be measured. When a charged particle passes through a medium of refractive index n with a velocity $\beta c > \frac{1}{n}$ greater than the local phase velocity of light in the medium, it emits Čherenkov radiation. The angle θ_C in which Čherenkov radiation is emitted, relative to the particle's direction, is given by

$$\cos \theta_C = \frac{1}{\beta n}. \tag{2.17}$$

Since for fixed momentum $p_0 = \beta\gamma mc$ the velocity of particles varies for particles with different masses, Čherenkov counters can be used to provide information for the identification of particles.

Chapter 3

Experimental Techniques and Methods

3.1 The ALICE IROC-Prototype

To demonstrate that the MWPC readout of the TPC can be replaced with GEM foils, a full size IROC prototype was built based on a spare MWPC-IROC of the ALICE TPC with the wire grids replaced by GEM foils [36]. The prototype is a trapezoidal-shape chamber, that is 497 mm long and between 292 and 467 mm wide. It consists of 4 components, which are shown in figure 3.1: GEM stack, pad plane, insulation plate and an aluminium frame. Below the GEM stack responsible for gas amplification, there is a pad plane with 5504 4 mm × 7.5 mm pads, made of a multi-layer Printed Circuit Board (PCB). A 3 mm Stesalit insulation plate separates the pad plane from the aluminium frame.

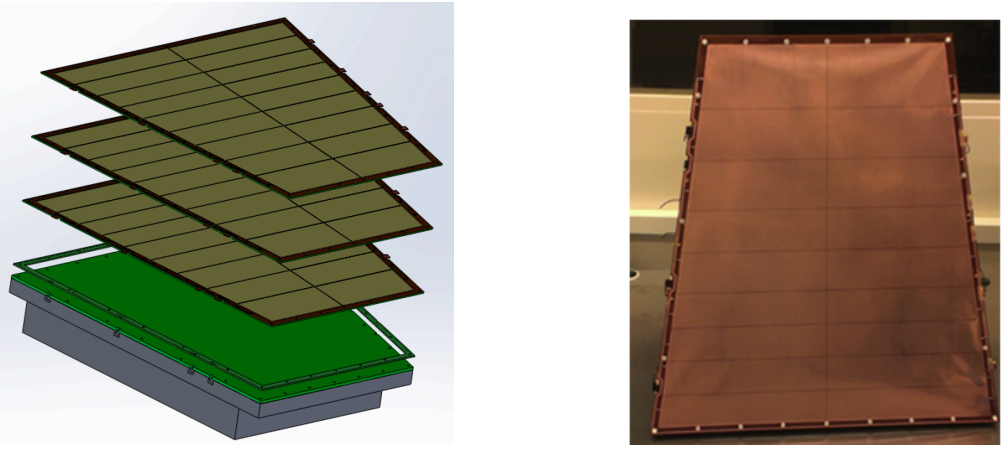

Figure 3.1: Exploded view of the mounted IROC prototype with triple GEM stack, pad plane and IROC aluminium frame and GEM stack mounted on aluminium frame [36].

GEM foils

The GEM foils used in the prototype were manufactured at CERN using a single mask etching technique, which is less precise than the double-mask process but unavoidable due to the large size of the foils [36]. The nominal diameters of the GEM holes are 50 µm for the inner hole and 80 µm for the outer hole, while the pitch between holes is 140 µm. An optical quality check confirmed the hole size to be 40 µm to 50 µm and 70 µm to 80 µm respectively [36]. The top side of a trapezoidal foil is segmented into 18 individually powered sectors with an inter sector spacing of 400 µm, which corresponds to the thickness of the spacer grid. Between the edges of the sector and the active area there is an additional 100 µm of copper to account for misalignments and to avoid holes directly at sector borders. The bottom side of a foil is unsegmented and can be directly connected to the High Voltage (HV) supply, whereas the top side is powered in parallel via loading resistors soldered directly on the foil between HV distribution path and the sectors. The mechanically stretched foils are glued on 2 mm fiberglass (G10) frames which contain a 400 µm spacer grid aligned with the sector boundaries to keep the GEM foils at a 2 mm distance. An additional frame is glued between the bottom GEM foil and the padplane increasing the induction gap to 4 mm. The GEM foils are mounted in the stack with the unsectored side of the GEM foils facing the padplane.

Padplane

The padplane consists of a multi-layer PCB, where 5504 pads are ordered in 63 rows with 68 to 108 pads per row. Because of the trapezoidal shape, the pad's geometry varies from rectangular pads in the center of the padplane to tetragons resembling parallelograms near the borders of the pad plane, as can be seen in figure 3.2. The position of the p-th pad in row r with N_r pads in the row is calculated in the local coordinate system of ALICE with the interaction point in the center of the ALICE TPC as the origin:

$$x(r,p) = (852.25 + 7.5r)\,\text{mm} \qquad y(r,p) = (4p + 2 - 2N_r)\,\text{mm}. \tag{3.1}$$

Test box with field cage

The chamber was mounted in the test box depicted in figure 3.3, which contained a drift electrode made of 50 µm aluminized mylar foil and a rectangular field cage consisting of 8 field-defining strips with 15 mm pitch and total dimensions of 57 cm × 61 cm. Between each of the strips a 1 MΩ resistor was placed. The last strip of the field cage was positioned 1 mm below the level of the first GEM foil in the stack and can be adjusted to match the drift field at the top electrode of the first

Figure 3.2: View of the pad plane

GEM by applying a voltage. The last strip is grounded by a 3.3 MΩ resistor. As can be seen in figure 3.4, the drift distance from the cathode to the first GEM is 10.6 cm. Mylar windows were machined in the walls of the test box for beam and radioactive source measurements.

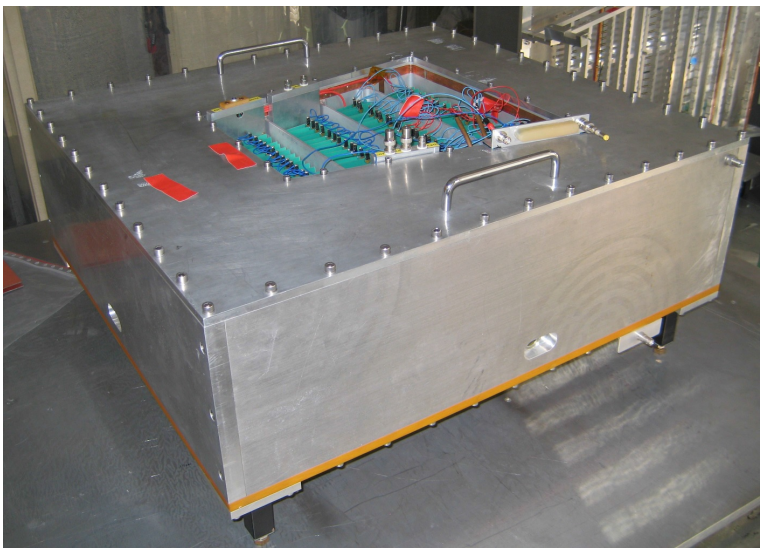

Figure 3.3: Test box with mounted ALICE IROC-prototype [36]

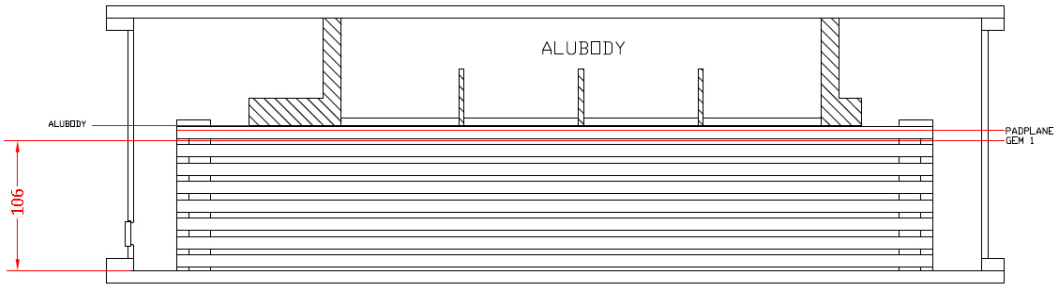

Figure 3.4: Cross section of the test box with mounted IROC prototype and field cage. The positions of the first foil in the GEM-stack, as well as the positions of the padplane and of the top of the aluminium frame (alubody) are marked with red lines and labeled. The drift distance is 106 mm [36].

High Voltage supply and settings

The prototype is powered using an ISEG HPn300 30 kV module for the cathode voltage and an ISEG EHS 860n 8-channel 6 kV module for the 3 GEM foils and the last strip of the field cage. The prototype was operated at different HV settings:

- **Standard settings**: The standard voltage settings are the ones typically applied in triple-GEM detectors, allowing the highest amplification to take place in the first GEM in order to provide maximum stability against discharges. The settings were inherited from the COMPASS experiment, but due to the

usage of a Ne-CO_2 (90/10) gas mixture in the prototype instead of Ar-CO_2 (70/30) as in the COMPASS experiment, all voltages in the GEM stack were scaled down by a factor of $69, 70, 71, 72, 73(\%)$.

- **Ion Backflow (IBF) settings**: These field configurations are aimed at the minimization of backdrifting ions in the drift region, since the charge amplification by avalanche formation happens mainly in the third GEM for these settings. The GEM voltages can be scaled to vary the total gain by a factor of $100, 103, 105, 107(\%)$. Furthermore the electric field between second and third GEM (Transfer Field 2) could be set to the values 200 V/cm, 400 V/cm, 600 V/cm and 800 V/cm. In contrast to standard settings, IBF settings may cause stability issues resulting in trips in the detector.

The standard drift field of the ALICE TPC of 400 V/cm was used for the prototype with the potential on the last strip of the field cage being kept at the same level as the top electrode of the top GEM foil's potential. The HV settings for the prototype are shown in table 3.1 .

	standard settings	IBF settings
drift field	0.4 kV/cm	0.4 kV/cm
ΔU_{GEM1}	400 V	225 V
TF1	3.73 kV/cm	3.8 kV/cm
ΔU_{GEM1}	365 V	235 V
TF2	3.73 kV/cm	0.2 kV/cm adjustable
ΔU_{GEM1}	320 V	285 V
induction field	3.73 kV/cm	3.8 kV/cm

Table 3.1: Voltage settings for the ALICE IROC prototype

3.2 Data Sample

3.2.1 Experimental set-up

The GEM IROC prototype was placed in the T10 beam line at Proton Synchrotron (PS) at CERN in the PS East Area experimental hall. The T10 beam is a secondary beam delivering secondary particles like electrons and pions and is derived from the 24 GeV/c primary PS beam. The test beam delivered either e^+ and π^+ or e^- and π^- with momentum ranging from 1 GeV to 6 GeV. The GEMs were powered

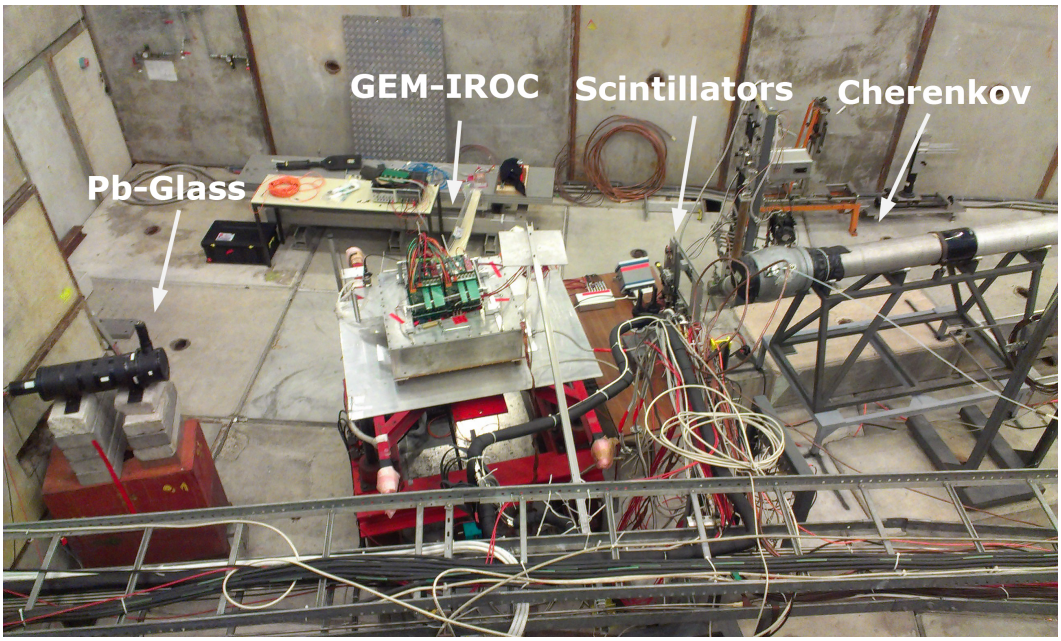

Figure 3.5: Experimental set-up for dE/dx performance measurements of the ALICE IROC prototype at PS East Area T10 beamline [36].

with standard and IBF optimized voltage settings for each type of beam. The drift velocity of the Ne/CO_2 (90/10) gas mixture in this configuration is 2.73 cm/µs. With a sampling frequency of 20 MHz the time invervall between two samples is 50 ns. A sample corresponds to a drift length of 1.365 mm [36].

The experimental setup is shown in figure 3.5. Two scintillation detectors were used for beam definition. A beam Čherenkov counter and a Pb-glass calorimeter were used as a reference during the test beam to provide PID capabilities, since no identification was possible with the IROC due to the absence of a magnetic field. The beam Čherenkov counter was installed in front of the prototype. It consisted of an aluminium tube with a diameter of 20 cm, that was filled with nitrogen at atmospheric pressure and was equipped with UV sensitive photomultipliers. The Pb-glass calorimeter was installed behind the prototype for additional electron/pion separation and to give additional information on particles passing the prototype. Since part of the electrons gave a significantly smaller signal in the Pb-glass calorimeter only the information of the Čherenkov counter was used for particle identification. The smaller signal in the Pb-glass calorimeter arose from misalignment of this detector to the rest of the set-up.

The prototype was equipped with 10 EUDET Front End Cards (FEC) [24] corresponding to about 1200 channels [36]. The card included a PCA 16 programmable

charge preamplifier, the digitization and signal processing was done with an ALTRO chip. The FECs were reading out signals from 16 to 18 pads on all 63 padrows of the padplane, corresponding to a width of the readout region of 6 cm to 7 cm, which is depicted in figure 4.1 [36]. The shaping time of the system was 120 ns, with a sampling frequency of 20 MHz this corresponds to 2.4 samples. The system had an RMS noise of around 600 electrons. The zero supression threshold was 2 ADC counts corresponding to about 1200 electrons with a conversion gain of 12 mV/fC [36]. The FECs were read out using the readout system currently used in the ALICE detector with two ALICE TPC readout control units sending the acquired data to a local data concentrator PC, which contained the recieving ReadOut Reciever Card and runs the ALICE data acquisition software DATE. A local trigger unit and a busy box handled the corresponding trigger logic. Data transfer and trigger communication were based on optical links. The readout of beam detectors, scintillators, Čherenkov counter and Pb-glass calorimeter was done via a classic CAMAC system into a PC running a LabView acquisition system. A busy logic implemented in the CAMAC system was responsible for synchronizing the events. Subsequently the data streams were merged into a single data file based on the proper synchronization of the trigger and an event tag [36]. The average data acquisition rate was 500 events/spill for a beam intensity of about 2000 particles/spill [36].

3.3 The TPC Reconstruction Chain

In this section the steps of the track feature extraction from signals of the ADCs connected to the single pads to tracks of particles traversing the TPC will be presented. The reconstruction of particle tracks is done in context of the software framework fopiroot, which was written and implemented in the C++ programming language. fopiroot is based on the FairRoot [4] package developed at GSI, Germany, which is an extension of the ROOT framework developed at CERN [19]. The reconstruction is done by tasks that can conveniently be run from macros. The reconstruction chain is shown in figure 3.6.

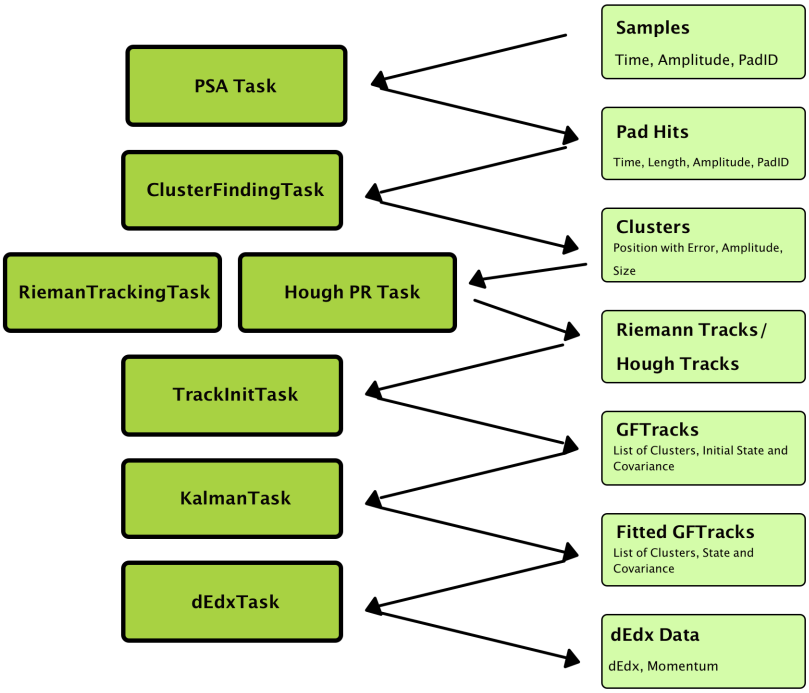

Figure 3.6: Structure of the reconstruction chain

3.3.1 Pulse Shape Analysis

The Pulse Shape Analysis (PSA) is the first algorithm that processes data from single readout pads. It combines consecutive data samples to a pad hit and assigns

it a time and an amplitude. The PSA searches the samples for local minima, local valleys or samples below a certain threshold, where it divides samples into pulses. Such a pulse is processed and assigned an amplitude A, which is defined by the sum of all amplitudes of the samples in the pulse and a time, to be stored as a pad hit:

$$A_{\text{pad hit}} = \sum_i A_{\text{sample } i} \qquad t_{\text{pad hit}} = t_{\max} - t_{\text{shaping}}. \tag{3.2}$$

The identification number of the pad (pad ID) is also stored with the pad hit to determine the position of the pad in the detector and obtain spatial informations for clustering finding. The time determination can be accomplished in different ways. The simplest way is to define the time of the pad hit t by the time of the sample with the maximum amplitude, shifted backwards in time by the peaking-time of the signal shaper $t_{\text{shaping}} = 120\,\text{ns}$. Another method called constant fraction discriminator which is used in the electromagnetic calorimeter trigger of the COMPASS [21] was also implemented. The algorithm calculates the difference between a pulse and a

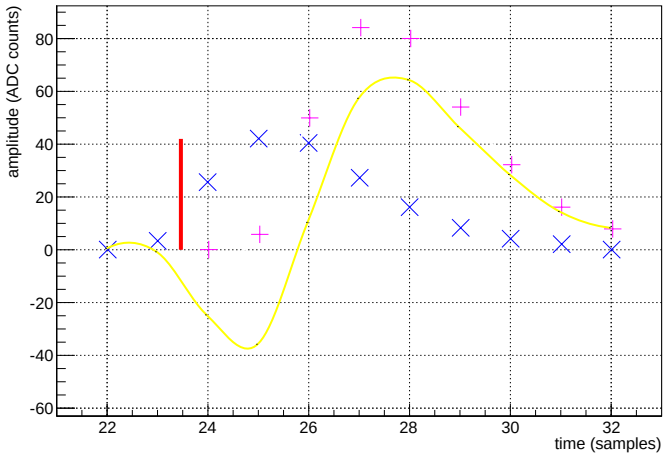

Figure 3.7: Constant Fraction Discriminator (CFD): The original signal is shown in blue crosses, the delayed signal in pink crosses and the difference between both signals in yellow. The time of the pad hit assigned by the CFD is shown by a red line, which is obtained by subtracting a calibration constant from the time, where the difference between delayed signal and signal crosses the abscissa axis.

delayed and amplified version of the pulse. To obtain the time of the pulse, the point where the linear interpolation of the difference between pulse and amplified pulse crosses the axis is calculated. From this point a calibration constant is subtracted and this value is assigned as the time of the pulse.

3.3.2 Cluster Finding

The Cluster Finder [34] takes the pad hits and combines hits that are likely to correspond to a common primary ionization to a cluster. Locally adjacent hits are grouped into a cluster, based on the information provided in a pad plane which represents the spatial distribution of the pads in the x- and y-plane. The time signal of a pad hit corresponds to the z-coordinate of the signal. First the algorithm sorts all pad hits in a certain timeslice by decreasing amplitude. Starting with the pad hit with the highest amplitude, it loops over pad hits and checks each pad hit against all clusters created until then. The cluster finder combines adjacent pads only, if the pad hits come from the same pad or neighbour a pad of any unsplit pad hit already in the cluster and if in addition the processed pad hit is within a certain time slice of the center of gravity in the cluster. If no matching cluster is found, a new cluster is created from the pad hit. If a pad hit matches more than one cluster, its amplitude is split between the matching clusters. From the pad hits assigned to a cluster the amplitude of that cluster is calculated by the sum of its pad hit amplitudes. The cluster is assigned a position by a weighted mean method:

$$\boldsymbol{x}_{\mathrm{Cl}} = \frac{\sum_{\text{pad hits}} \boldsymbol{x}_{\text{pad hit}} \cdot A_{\text{pad hit}}}{\sum_{\text{pad hits}} A_{\text{pad hit}}}. \tag{3.3}$$

The quantity $\boldsymbol{\sigma} = (\sigma_x, \sigma_y, \sigma_z)$ describes the cluster's spatial error. It is estimated from the standard deviation of the signal positions weighted with the cluster's amplitude A_{Cl}. By dividing the variance by the amplitude, which is proportional to the number of ionization electrons, the reduction of the statistical fluctuations from electron drift is taken into account[1]. An arbitrary factor C was introduced to scale the errors to an appropriate size. The variance and σ_i is calculated as

$$\mathrm{Var}_i = \frac{1}{A_{\mathrm{Cl}}} \sum_{\text{pad hit}} A_{\text{pad hit}} (\boldsymbol{x}_{\text{pad hit},i} - \boldsymbol{x}_{\mathrm{Cl},i})^2 \tag{3.4}$$

$$\sigma_i = \frac{C}{A_{\mathrm{Cl}}} \cdot \sqrt{\mathrm{Var}_i}. \tag{3.5}$$

For clusters consisting of one hit, $\boldsymbol{\sigma}$ is calculated as

$$\sigma_i = \frac{C}{A_{\mathrm{Cl}}} \cdot \sqrt{\frac{d_i}{12}}, \tag{3.6}$$

where d_x and d_y denote the length and wide of a pad and d_z the jitter in z. A two dimensional clustering in padrows and time has been implemented by restricting the

[1] The error should then be calculated as $\sigma_i = C \cdot \sqrt{\frac{\mathrm{Var}_i}{A_{\mathrm{Cl}}}}$. However in the code it was implemented as written in the text. Since the arbitrary factor C introduces a large systematic uncertainty this problem is estimated to have a minor effect. The algorithm should be revised.

existing clustering algorithm to search for adjacent pad hits only in the same padrow and in time.

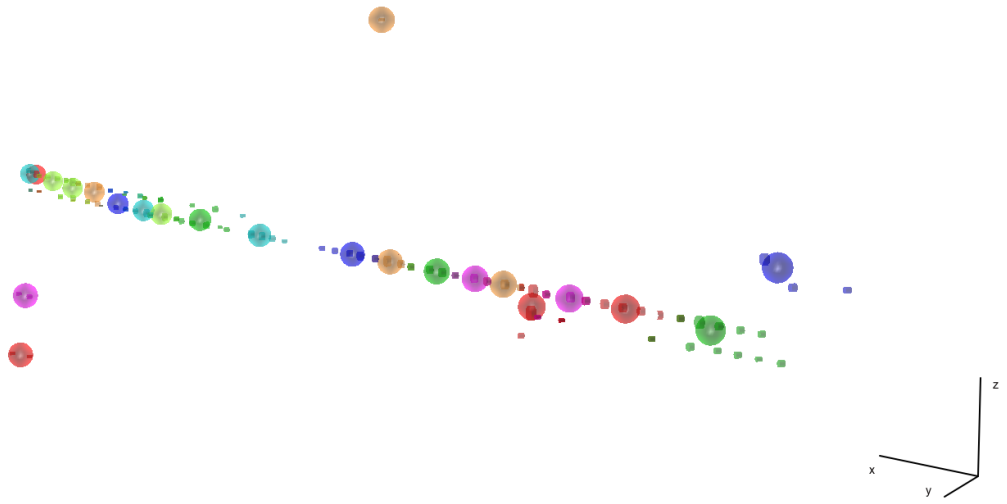

Figure 3.8: Illustration of the 3D cluster finding algorithm working on event 15 in run 681, pad hits (shown as cylinders) are grouped as clusters (shown as spheres). A cylinder's radius is proportional to the digi amplitudes in a logarithmic scaling.

3.3.3 Pattern Recognition

In order to reconstruct the trajectories of particles passing through the detector, a Pattern Recognition algorithm has to group clusters, which originate from a single physical track. Usually in a particle physics experiment, the pattern to be recognized are helices, assuming helical trajectories of charged particles in a homogenous magnetic field. For this analysis however, due to the absence of a magnetic field, the pattern to be recognized are straight lines. The framework provides two different algorithms: A Riemann track follower [34] fitting helices to a set of hits by an extended Riemann fit and a Hough Transform Pattern recognition algorithm [17]. The Riemann Pattern Recognition is used in the final analysis, because of its better performance with the 2 dimensional clustering.

The Riemann Pattern Recognition algorithm associates three dimensional space points provided by the clusters to tracks for which a helical shape is assumed. A helix is fitted to a set of hits by an extended Riemann fit. This fit makes use of the Riemann Transformation, a stereographic projection mapping a plane onto the so-

called Riemann sphere with diameter of 1 on top of the origin of the complex plane. The Riemann Transformation maps circles and straight lines on the plane to circles on the sphere corresponding to planes in space, thus reducing the challenging task of circle-fitting on the plane to the task of plane-fitting on the Riemann sphere. The Riemann sphere is scaled to appropriate size with respect to the detectors geometry. After the fast fitting algorithm, the hits along the track are sorted properly and estimates of the track parameters are provided to the fitting algorithm to reconstruct particle trajectories. A schematic of the algorithm is shown in figure 3.9. The

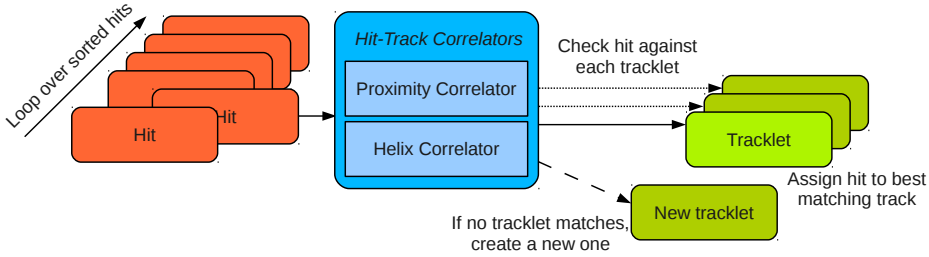

Figure 3.9: Scheme of the track building process with the Riemann track follower [34]

algorithm starts with a first tracklet which contains only one hit, then the presorted clusters are looped and each hit is checked against each existing tracklet. If both hit-track correlators are matched, the hit is assigned to the best matching tracklet. A matching correlator delivers a matching quality. Two correlators are applied:

- A proximity correlator checks the proximity of a cluster to a track by finding the nearest cluster in the tracklet and delivering the distance between those clusters as a matching quality.
- A helix correlator calculates the distance between the cluster and the helix defining the tracklet. By Newton's method, the minimum distance is found and delivered as a matching quality.

If the matching quality of a correlator is smaller than a definable cut, the tracklet survives the correlator, otherwise if no tracklet matches a hit, a new tracklet is created. If the root mean square of the tracklet's hits to the fitted helix is less than a definable cut, then the tracklet is stored and can be further processed. Due to outliers, noise hits, incorrectly assigned hits, fragmentary tracks of particles with low energy loss and even defect readout channels, the actual tracks might not be found as a whole in the process of track building. Because of that, a second level tracklet merging is performed, where the tracklets are presorted and compared to

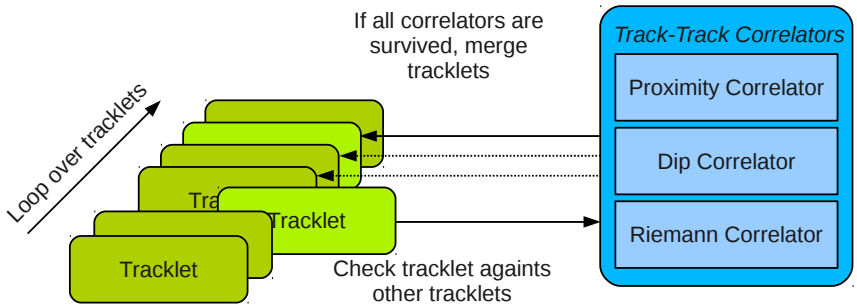

Figure 3.10: Scheme of the track merging process [34]

each other. The track merging algorithm is shown schematically in figure 3.10. Like in the track finding process certain track-track correlators have to be matched in order for two tracks to be merged:

- A proximity correlator compares the position of the first and last hits of the two tracklets. If the distance between the position of the hits is smaller than a definable proximity cut, the proximity correlator is survived.
- A dip correlator compares the dip angles of the two tracklets, which are defined as the angle between a line parallel to the z-axis and a tangent on the helix of a track. If the relative z-positions of the tracks match and the absolute difference of the dip angles is smaller than the definable angle-cut, the dip correlator is survived.
- A helix correlator creates a new track temporarily containing the hits of both tracks. A helix fit is performed and a cut on the root-mean-square of the distance of the hits to the helix is applied. If the two tracks together do not have enough hits to be fitted, this correlator is not applicable.

3.3.4 Track Representation

The unfitted tracks found by the pattern recognition are parametrized in a 5 dimensional track parametrization in virtual detector plane coordinates with the state vector $p = (q/p, u', v', u, v)^T$. Here q denotes the particle's charge, p its momentum, u, v the position of its track on the (virtual) detector plane and u', v' the direction cosines of the track in the plane. Figure 3.11 shows a virtual detector plane as used in the GENFIT track parametrization. Further information on the treatment of tracks can be found in [23] and [34].

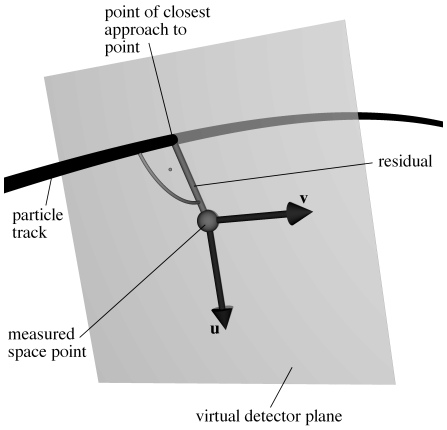

Figure 3.11: Virtual detector plane for a space point hit [23]

$$u = (\boldsymbol{x} - \boldsymbol{o}) \cdot \boldsymbol{u}$$
$$v = (\boldsymbol{x} - \boldsymbol{o}) \cdot \boldsymbol{v}$$
$$u' = \frac{\boldsymbol{a} \cdot \boldsymbol{u}}{\boldsymbol{a} \cdot \boldsymbol{n}}$$
$$v' = \frac{\boldsymbol{a} \cdot \boldsymbol{v}}{\boldsymbol{a} \cdot \boldsymbol{n}}$$

with $\boldsymbol{x}$: position in space in a master coordinate system, $\boldsymbol{a}$: direction of the track and $\boldsymbol{o}$: origin of the plane in a master coordinate system

The master coordinate system is defined by the ALICE local coordinate system of the IROC as introduced in figure 1.2.

3.3.5 Kalman Track Fitting

The Track Fitting is achieved with a Kalman filter [25] [34], an algorithm to produce an optimal estimate of a system state from a series of noisy measurements. It is implemented in GENFIT, a generic toolkit for track reconstruction for experiments in particle and nuclear physics [23]. Further information on the working principle of the Kalman filter can be found in [23].

3.4 Extraction of Specific Energy Loss Data

To extract specific energy loss data (dE/dx) from a track, a dE/dx task optimized for the detector geometry has been implemented in the analysis framework.

A reconstructed track is extrapolated to the first padrow of the detector. From there it is iteratively being extrapolated to the next padrow. The length of the track between two rows, calculated as the magnitude of the difference of the track's position at two neighbouring rows, is assigned as Δx. The sum of all pad hits in the respective padrow corresponding to the track is assigned as ΔE. The energy loss per

padrow $\Delta E/\Delta x$ is stored as a dE/dx sample, which is used in the calculation of the truncated mean.

A second version of the dE/dx task has also been implemented, where the summation over the pad hit's amplitudes is carried out in a region around the track instead over the amplitudes of pad hits assigned to the track by the pattern recognition. In this way possible deficiencies in the track finding algorithms can be overcome. The region around the track is defined by a rectangular box around the track with definable width and heigth.

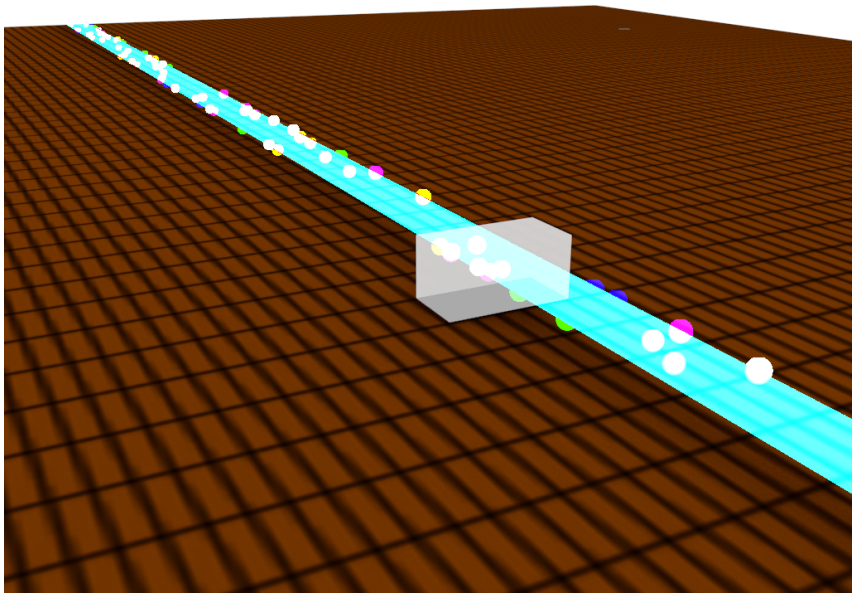

Figure 3.12: Illustration of the dE/dx task at work, the track (cyan) is extrapolated to the first padrow, from where the track is extrapolated iteratively to the next padrow. The pad hits (colored spheres) in the respective padrow in a region around the track (grey box) are summed up and together with the length of the track between two padrows they contribute to the specific energy loss.

Chapter 4

Results and Discussion

4.1 Data Selection

During the beam time, data was acquired during 84 runs, which are listed in the appendix A. To investigate optimal parameters for clustering and pattern recognition, run 681 with standard HV settings and 69% gain and run 694, with IBF HV settings (TF2: 800 V/cm) and 103% gain were selected as benchmarks in this analysis. In run 681 a total of 81 961 events was recorded, whereas in run 694 a total of 63 005 events was recorded. The gas amplification of the GEMs in run 681 was measured to a gain of 1500, whereas the gas amplification in run 694 was measured to a gain of 5200 [36]. In a first analysis the occupancy of pads was investigated to find pads with unusually many signals. The occupancy of pads is shown in figure 4.1 using a logarithmic scale. The boundaries of the IROC are drawn with black lines.

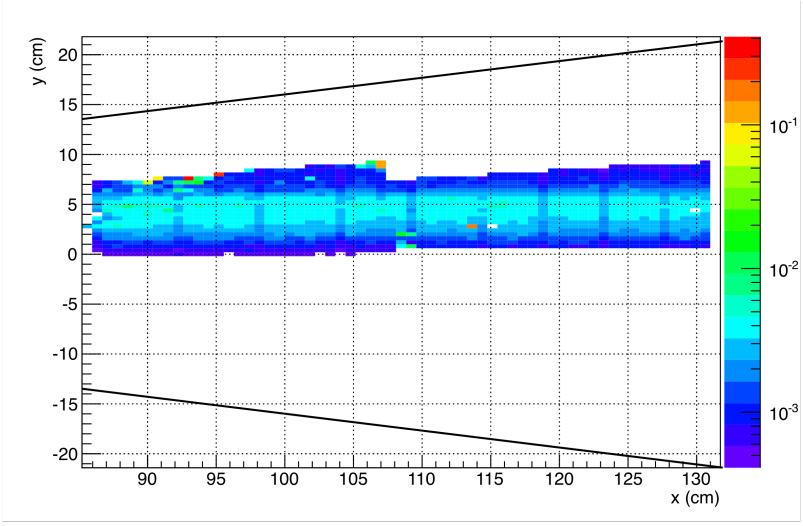

Figure 4.1: Occupancy map for run 681 with marked shape of the IROC.

The pads with the pad IDs 465, 537, 754, 978, 2271, 2272 and 3057 measured

unusually many signals, which indicated that mainly noise was measured with these channels. A comparision between the amplitude distribution of such a pad and a neighbouring pad, which measured a reasonable amount of signals is shown in figure 4.2. Since the noise significantly worsened the efficiency of the pattern recognition, these channels were excluded from the analysis. In further studies the effect of a suitable threshold for pad hits could be investigated.

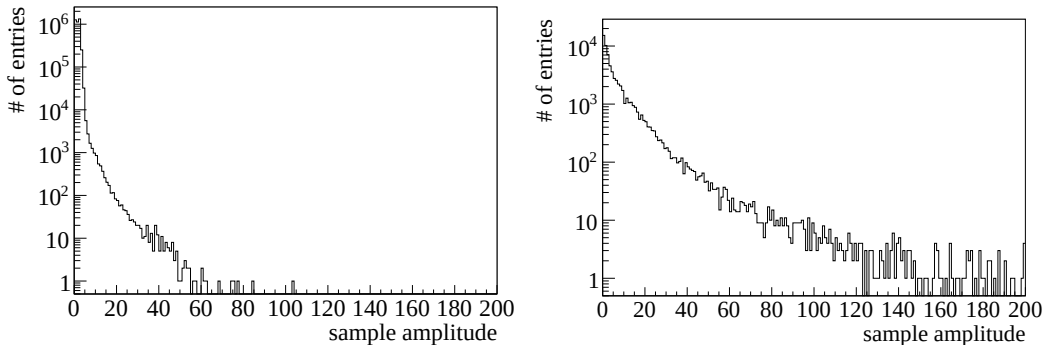

Figure 4.2: Comparision of the amplitude distributions for pad 3057 and pad 3056 in run 681

The readout window of the pads was much longer than the maximum drift time of particles in the test box, therefore only signals with time bin below a threshold of $t_{\text{cut}} = 4.5\,\mu\text{s}$ (90 samples) were considered in the analysis. A distribution of the sample's amplitudes and timestamps, which motivated the applied cut, can be seen in figure 4.3.

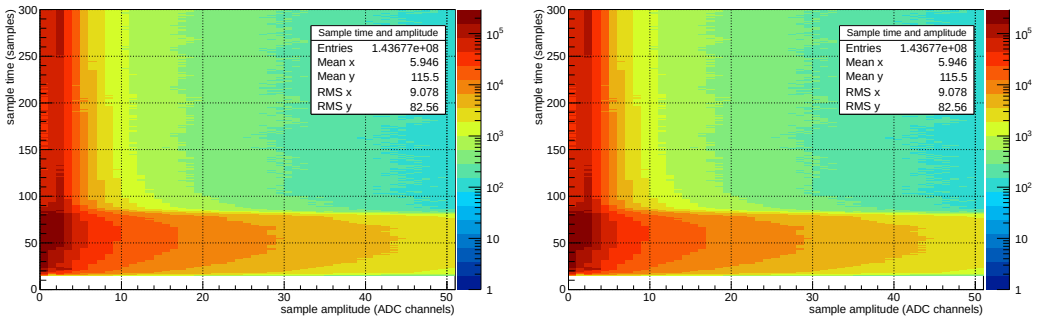

Figure 4.3: Distribution of sample timestamps and amplitudes for run 681 and 694

The gain correction obtained by the analysis of University of Tübingen, which was described in section 1.3, was applied to the samples' amplitudes.

Due to a bad connector in the experimental setup, the first 4 rows had to be excluded from the analysis. The last 3 rows were excluded from the analysis because the tracks seemed distorted on the edges, which was confirmed by the analysis of Martin Ljunggren [30] and can be seen in figure 4.4. The pattern recognition improved by excluding these rows.

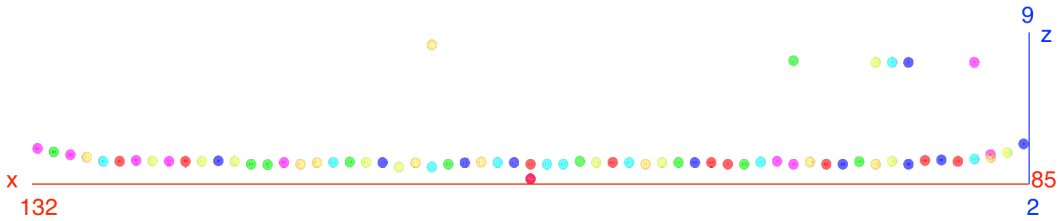

Figure 4.4: x- and z- cluster positions for event 33 in run 681

Because the Constant Fraction Discriminator, which was discussed in section 3.3.1, only worked on a fraction of the signals, the time of a pad hit was assigned by subtracting the shaping time from the timestamp of the maximum amplitude of the pulse. Otherwise a bias might have been intruduced by using two different time calculations. In figure 4.5 a pad hit extracted by the PSA is shown.

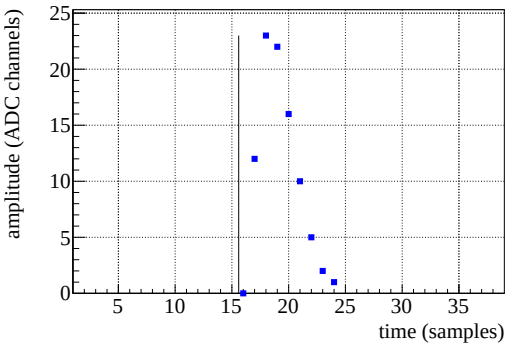

Figure 4.5: Pad hit extracted by the PSA algorithm, the time assigned to the pad hit is indicated by the black line

4.2 Track Reconstruction

Different reconstruction methods were tested for their capability of reconstructing particle tracks, which are needed for the dE/dx analysis.

The reconstruction, which was used in the dE/dx analysis, makes use of a two dimensional clustering in one row and time, as described in section 3.3.2. In contrast to 3 dimensional clustering, the determination of neighbouring pads was unambiguous, because despite the padplane's geometry, the left and right neighbour of a pad are well-defined. In the clustering a timeslice of $t_{\text{slice}} = 1.05\,\mu\text{s}$ (21 samples) was used for clustering in z-direction. The distributions of how many clusters were found in an event and how many clusters were found in events where the pattern recognition found one track, are shown in figure 4.6 for run 681.

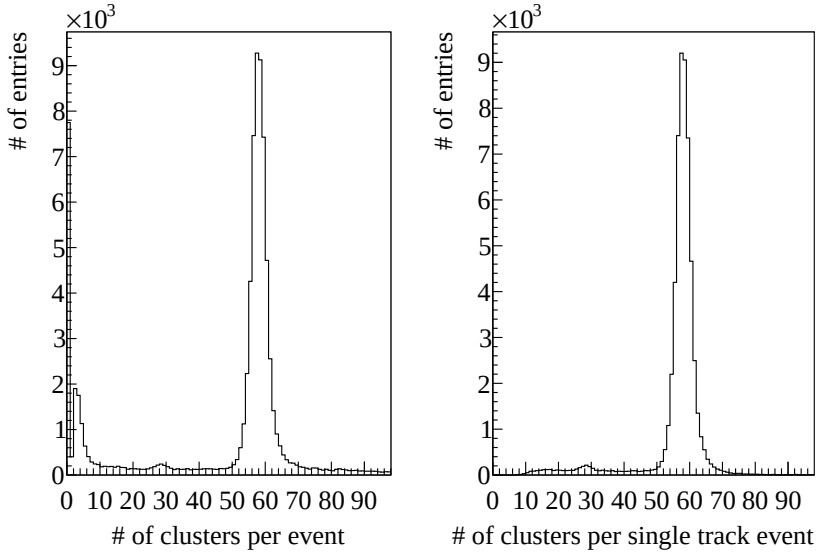

Figure 4.6: Clusters per event / single track event for run 681

As expected for 56 pad rows included in the analysis and the track extending over the rows, the distribution peaks at this value. Comparing both benchmark runs, run 694 has generally more clusters per event, which can be explained by the higher gas amplification. The average cluster size of a cluster is shown in figure 4.7 for run 681. The distributions of the cluster size in three dimensions and in two dimensions being very similar indicates, that most clusters consist only of one pad hit in z-direction. Due to the higher gas amplification in run 694, more clusters include pad hits two or more pads.

The pattern recognition was done with the Riemann Track Finder with the pa-

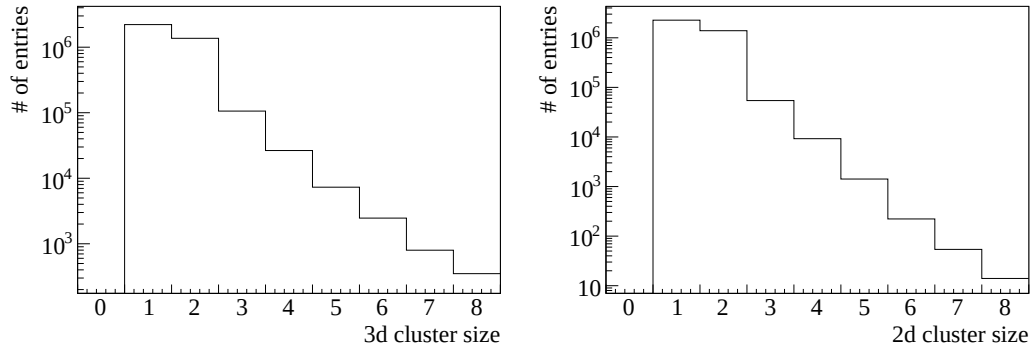

Figure 4.7: Cluster size in three dimensions and cluster size in two dimensions (x and y) for run 681

rameters listed in table 4.1, which were obtained by carefully tuning the cuts in a custom 3D event display. It was also used to create figures 3.8 and 4.10.

Table 4.1: Parameters of the reconstruction

Scaling factor of riemann sphere	80
Minimum number of hits for a helix fit	6
Cuts for the hit-track correlators	
Proximity cut	1.5 cm
Stretch of proximity cut in z	1.0
Helix cut	0.4 cm
RMS cut	0.4 cm
Cuts for the track-track correlators	
Proximity cut	5 cm
Dip angle cut	0.8 rad
Helix cut	2.0 cm
Helix RMS cut	1.0

The number of tracks found by the pattern recognition is shown in figure 4.8. The distributions for both runs being very similar in shape indicates that the pattern recognition works equally well for runs with different parameters.

The number of clusters per track is shown in figure 4.9. The small local maximum at 26 clusters per track can be explained with the geometry of the readout area which can be seen in the occupancy map in figure 4.1. Tracks crossing the IROC near the boundaries of the readout area are only registered up to $x < 107\,\text{cm}$, which results in a track extending only over half the readout area. The cutoff at 6 clusters per track originates from the cut parameter in the pattern recognition. The distributions for

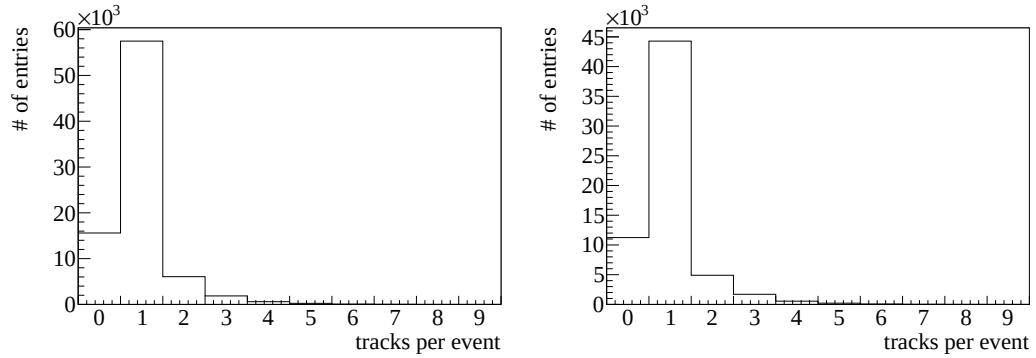

Figure 4.8: Number of reconstructed tracks per event for run 681 and run 694

run 681 and run 694 are very similar in shape both peaking at the expected value of 56 clusters per track. The peak of the distribution of run 694 is more narrow compared to run 681, indicating that in run 681 more tracks have gaps in them. A single track event and a multiple track event is shown in figure 4.10.

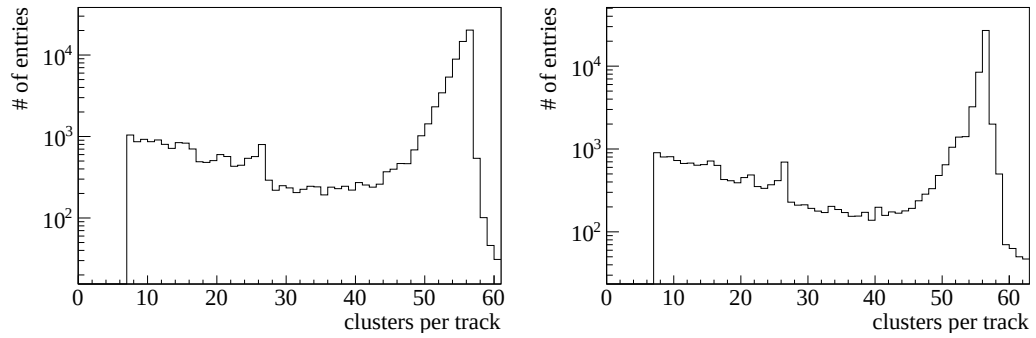

Figure 4.9: Number of clusters per reconstructed track for run 681 and run 694

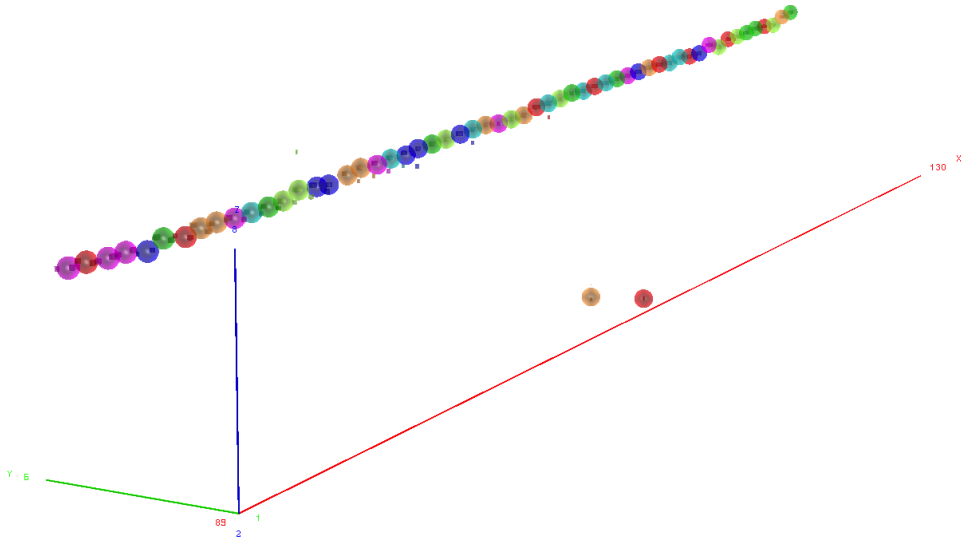

(a) Single track event (20)

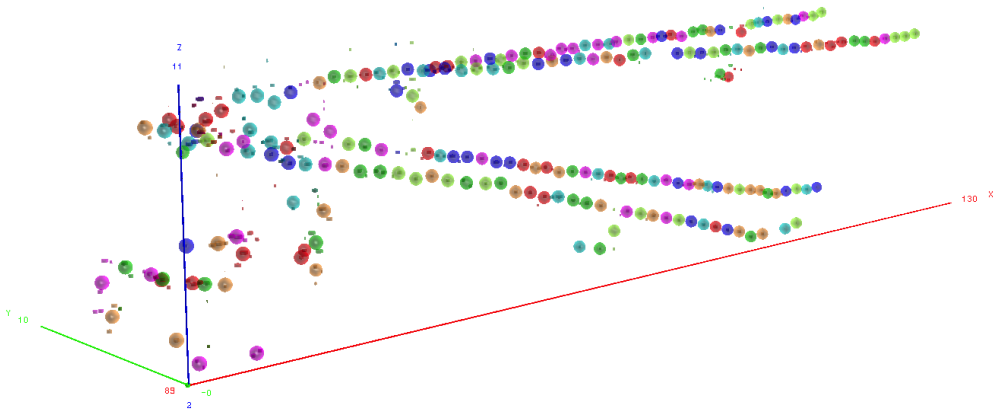

(b) Multiple track event (11)

Figure 4.10: Different types of events in run 681

The Kalman filter was applied with 2 iterations. The quality of the track fitting can be estimated on the basis of the track's residuals[1] shown in figures 4.12, 4.13, 4.14 and 4.15. The residual is defined as the distance from the track to a cluster.

The very narrow peak at zero in the y-residual can be explained with tracks extending over one pad per row, resulting in a near zero residual. The z-residual's asymmetric shape is not fully understood. For runs with higher gain the distribution becomes more symmetric. Probably the primitive time determination causes the asymmetric shape, which could be improved with further studies.

To obtain an estimate for the resolution of the detector from the residuals, three Gaussians were fitted to the distribution of the residuals. For the y-residuals the Gaussian $G1$ was used to describe the narrow peak, whereas for the z-residuals it was used to describe the peak's asymetry. Gaussian $G2$ and $G3$ were used to fit the shape of the residual. The resolution of the residuals was obtained by the means of the weighted mean of $G1$ and $G2$. The y-resolution was estimated to be 377.31 µm for run 681 and 312.19 µm for run 694. The resolution for run 694 is better because of the larger cluster size in this run. The resolution of the z-residuals was estimated to be 546.33 µm for run 681 and 614.63 µm for run 694. The space point resolution of the ALICE TPC in z for the test box drift length was measured with cosmics to be 350 µm [7].

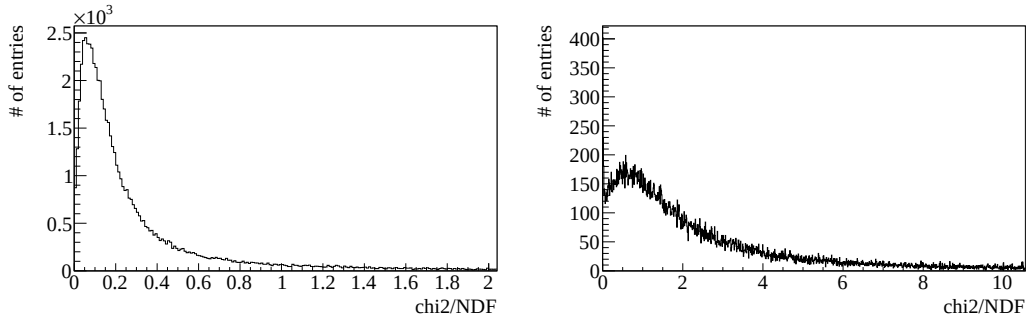

Figure 4.11: χ^2/NDF distribution of the reconstructed tracks for run 681 and 694

The χ^2/NDF distribution shown in figure 4.11 is an indicator for the quality of a fit and is expected to peak at 1, if the error estimation was done correctly. Despite the biased error on the cluster position, the distributions show the expected shape, but do not peak at 1. The difference between the distributions for runs with low and high gas amplification shows, that the error calculation is done incorrectly. Further work is necessary to calibrate the error calculation.

[1] By mistake the residuals were biased by including the cluster for which the residual is calculated in the fit of the track. Since most tracks consist of 56 clusters, the effect should not bias the residuals much.

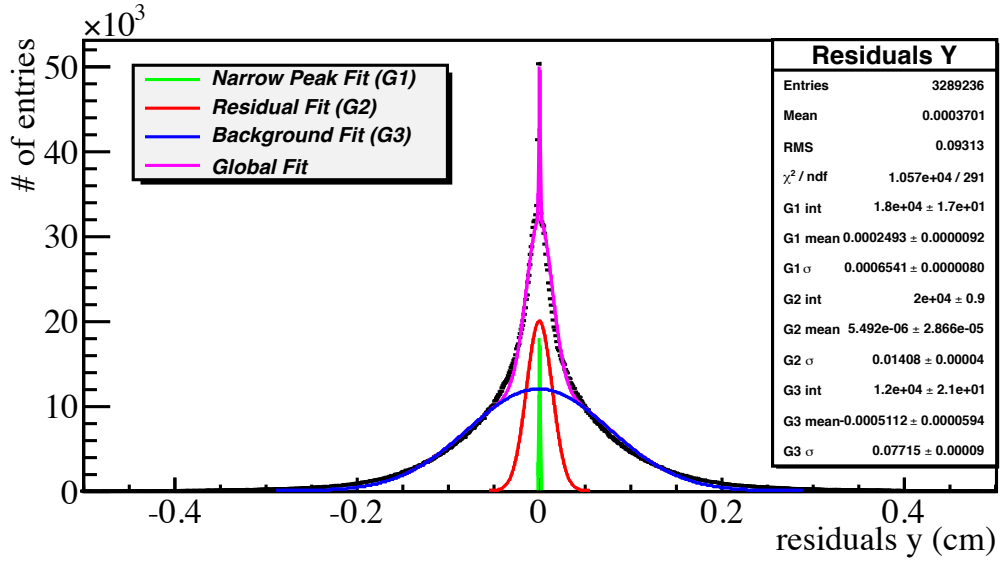

Figure 4.12: y-residuals of the reconstructed tracks for run 681

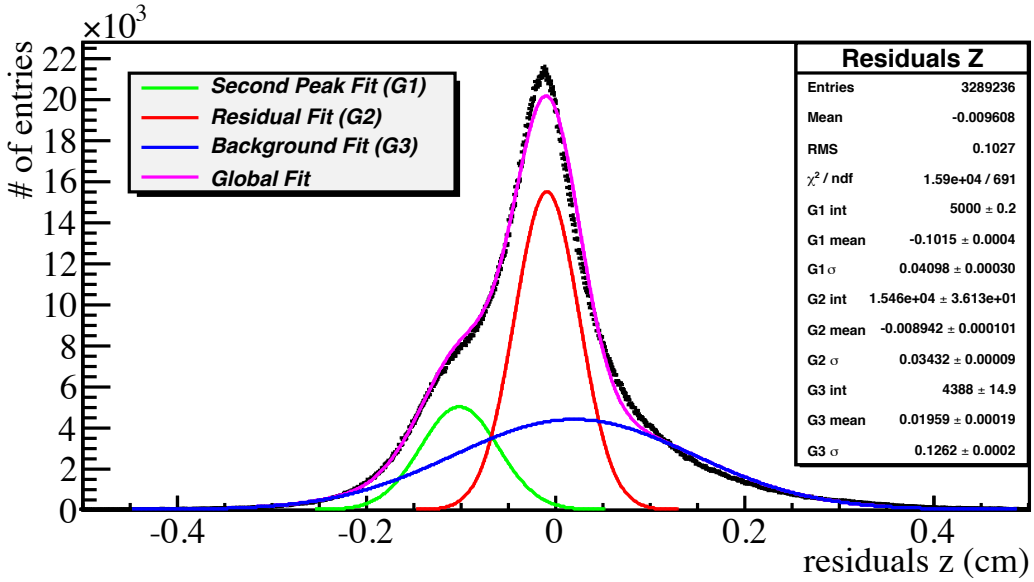

Figure 4.13: z-residuals of the reconstructed tracks for run 681

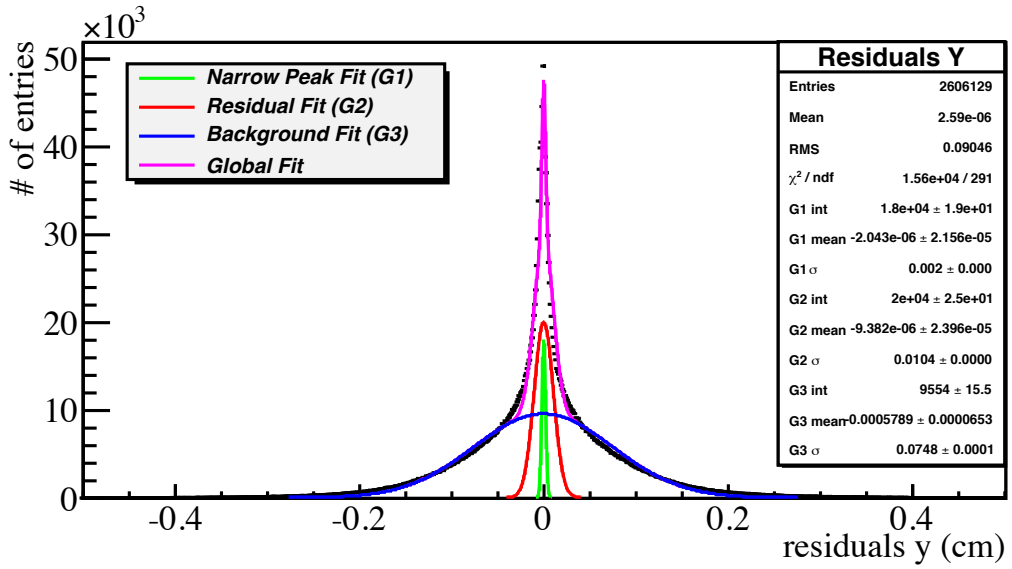

Figure 4.14: y-residuals of the reconstructed tracks for run 694

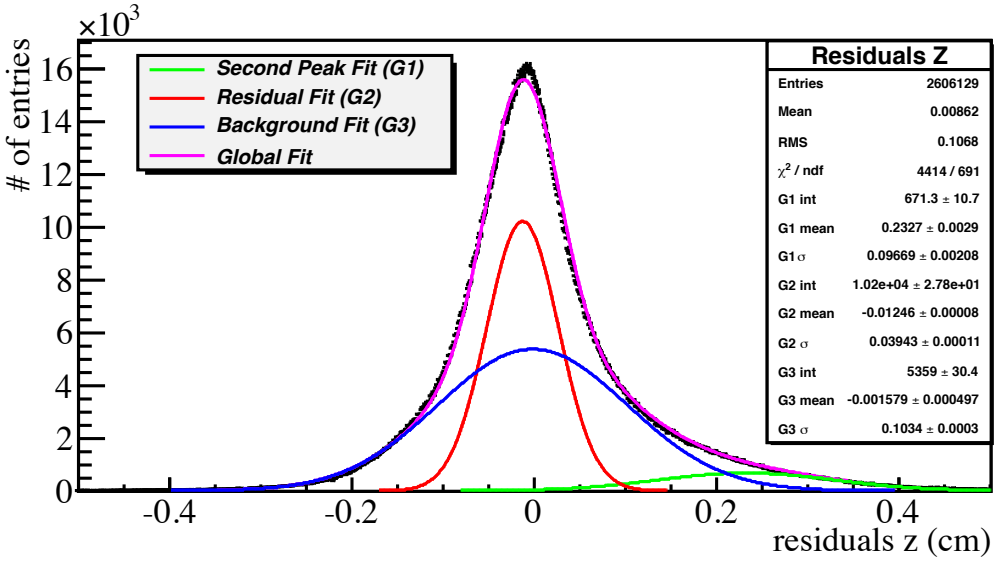

Figure 4.15: z-residuals of the reconstructed tracks for run 694

The distributions of the reconstructed track's angles in the x-y-plane with respect to the x-axis (ϕ) and in the x-z-plane with respect to the x-axis (θ) are shown in figure 4.16 for run 681. The distribution of the track parameters of run 694 resemble those of run 681. The distributions show a very narrow peak, indicating that most tracks are almost parallel to the x-axis. In the ϕ distribution however one observes an additional peak at 0.012 rad. The origin of the peak could not be fully reasoned out. Because the track parameters of tracks with $\phi > 0.005$ rad revealed no inconsistencies, these tracks were included in the dE/dx analysis.

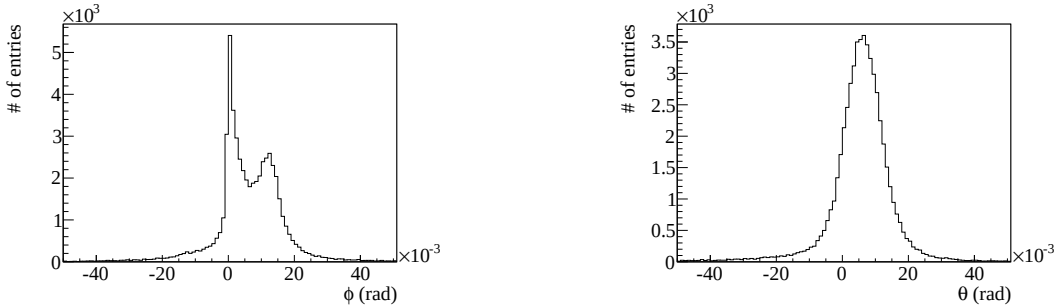

Figure 4.16: Distribution of the angles ϕ and θ of single tracks for run 681

In figure 4.17 the distributions of the fitted tracks' y- and z-positions at the starting point of the fit are shown for run 681. The distinctive spikes in the distributions of the y-positions are caused by straight tracks that only extend over one pad per row. The asymetric shape of the distribution originates in the geometry of the readout region, which can be seen in figure 4.1. The peak in the distributions of the z-positions at 1.8 cm was excluded in the analysis of University of Tübingen. To be able to compare the results, the peak was also excluded in this analysis.

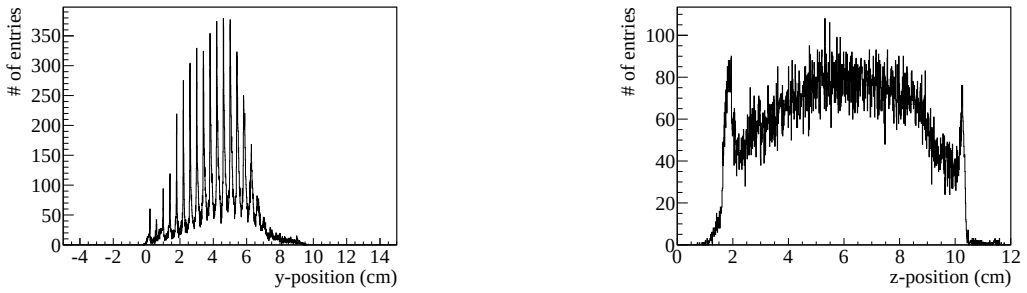

Figure 4.17: Distribution of single track start positions in y and z for run 681

4.3 Energy Loss Spectra

4.3.1 Data selection

By restricting the analysis to single track events, the PID capabilities of the additional detectors could be utilized. The signal of the Čherenkov counter was used to distinguish electrons from pions, which is shown together with the signal of the Pb-Glass detector in figure 4.18. Single track events with a signal greater than 400 in the Čherenkov counter were interpreted as events with an electron, whereas single track events with a signal lower than 150 in the Čherenkov counter were interpreted as events with a pion.

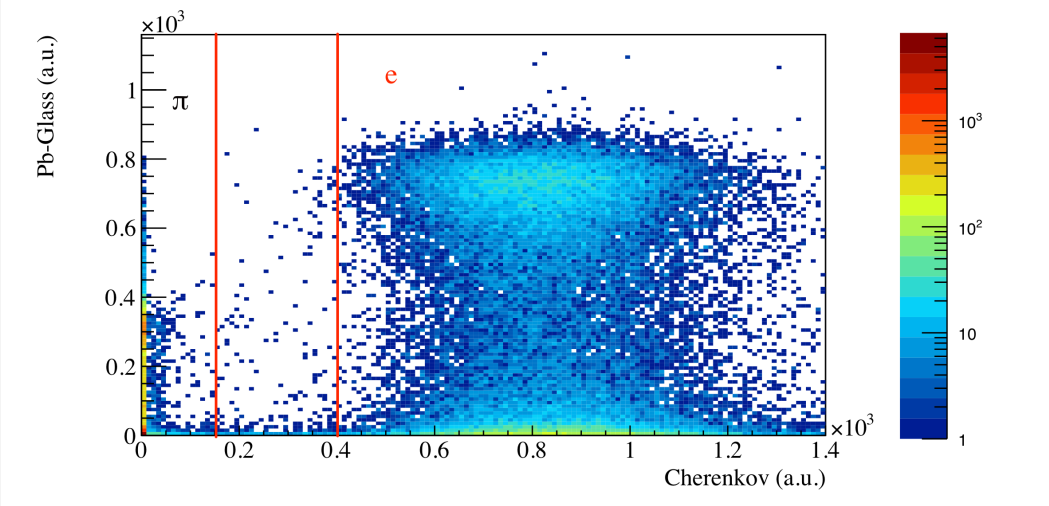

Figure 4.18: Signal from the Čherenkov counter and signal from the Pb-Glass detector, PID cuts are indicated by red lines.

For the dE/dx-analysis only tracks with a sum of their dx samples $> 35\,\text{cm}$ were considered, in order to exclude incomplete and small tracks. In figure 4.19 the distributions of the sums of the dx-samples are shown for run 681. The distributions for other runs were similar in shape.

Only tracks whose z-position at the beginning of the track was in the interval 2.7 cm to 10.6 cm were considered in the analysis. The lower limit was chosen to be able to compare with the Tübingen analysis and the upper limit was chosen because of the maximum drift length of the detector.

The dE/dx task which collected all pad hits in a definable region around the track was used for the creation of dE/dx samples. By collecting all samples in an area around the track instead of only processing the samples assigned to the track, it is guaranteed that no sample amplitude and therefore no primary charge will be lost

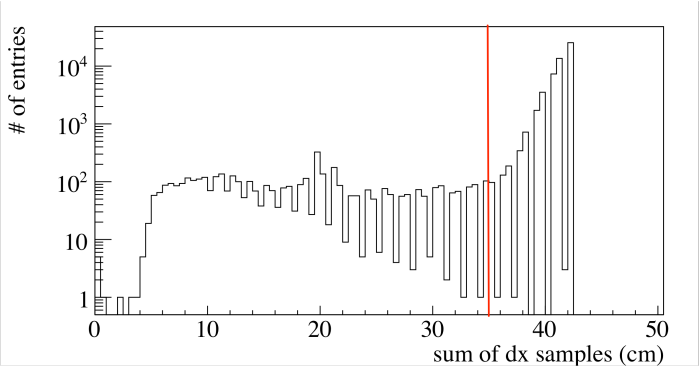

Figure 4.19: Distributions of the sum of dx samples for run 681 with cuts indicated by red lines

due to perhaps an insufficient pattern recognition. A collection region of a square of $2\,\text{cm} \times 2\,\text{cm}$ around the track turned out as the best parameter.

4.3.2 Method of the Truncated Mean

The energy loss spectra were obtained by the method of the truncated mean because of the long tail of the straggling function. A certain fraction of the lowest and/or highest values of the dE/dx samples is discarded before calculation of the mean, so that by calculating the truncated mean, the most probable value of the energy loss distribution is obtained. Although the amount of data is reduced by this procedure, the fluctuations of the mean values are kept to a minimum, as the outliers from the tail of the straggling function are omitted in calculating the mean value. By convention in this analysis, a truncation of $[5, 75]$ means that 5% of the lowest samples and 25% of the highest samples are discarded.

The truncations $[0, 75]$, $[5, 75]$, $[10, 75]$, $[0, 70]$, $[5, 70]$ and $[10, 70]$ were tested with a beam momentum of $1\,\text{GeV/c}$ for standard settings with different HV scale factors. The effect of the truncation settings on the energy resolution for electrons and pions is shown in figure 4.20 and 4.21. Based on the analyzed data one optimal truncation setting for all runs cannot be determined, as even for standard settings the best truncation settings vary for different HV scaling factors. However the choice of [10,70] seems promising for standard settings.

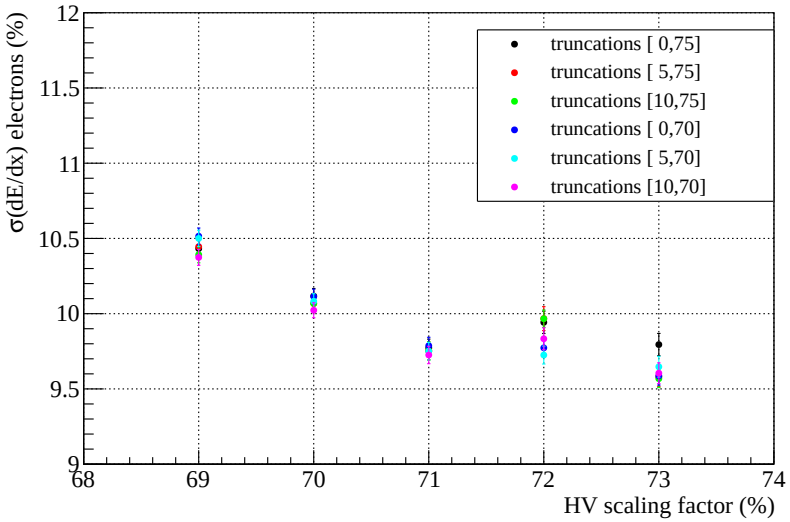

Figure 4.20: Electron energy resolution for different truncations (standard HV settings)

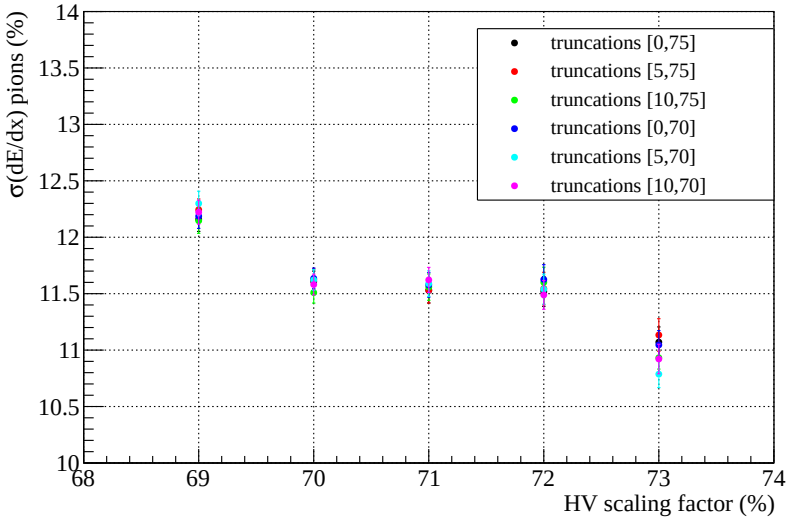

Figure 4.21: Pion energy resolution for different truncations (standard HV settings)

Findig the optimal truncations for all 103 runs can be investigated in further studies but is beyond the scope if this analysis. Since the choice of the truncations did not strongly alter the energy resolution, the truncations $[5, 75]$ were chosen to compare the results with those of University of Tübingen, which used the same truncations. The effect of the chosen truncations on a distribution of dE/dx samples of a single track can be seen in figure 4.22.

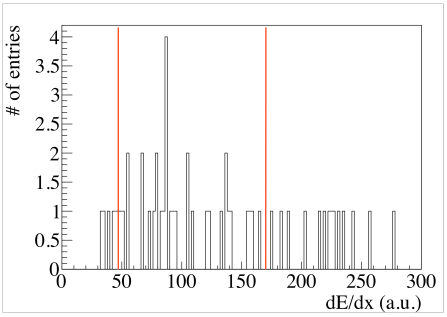

Figure 4.22: dE/dx samples from event 40 in run 681, truncations $[5, 75]$ indicated with red lines.

In figure 4.23 the energy loss spectra for standard HV settings, 1 GeV/c beam momentum with negative polarity are shown. The two peaks in the spectrum are due to electrons and pions. Electrons have a larger energy loss in matter due to their smaller mass and therefore a larger $\beta\gamma$ for fixed momentum. The peaks are fitted with a combined fit of two Gaussians (green) and a polynomial of the 4th order (purple) to describe the background. The fit area was limited to $\langle dE/dx \rangle_{\max} \pm 2\sigma(dE/dx)$.

Since the energy loss of the particle is independent of the gas amplification, the ratio of the gas amplification gain and the mean energy loss should be a constant for different HV scaling factors. For the standard HV settings with scaling factors 71 %, 72 % and 73 % an estimation with gains provided in [36] showed good agreement with figure 4.23. The relative resolution depends on the fluctuations in the primary particle's ionization, described by the straggling function, and the fluctuations in the gas amplification. The fluctuations of the straggling function, which are determined by the average number of primary inelastic collisions, usually dominate. One would expect the relative resolution to be independent of the gas amplification gain. However in figure 4.23 one observes a small improvement of the resolution for higher scaling factors, which could result from the loss of charge due to zero supression. Further studies could investigate the cause of this effect.

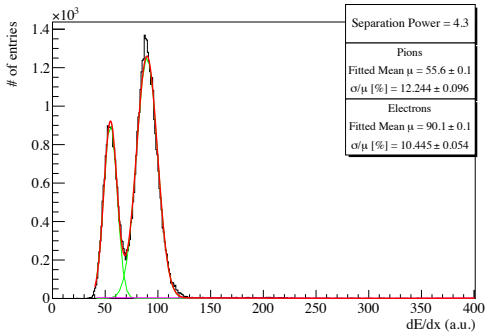

(a) 69 % HV scaling

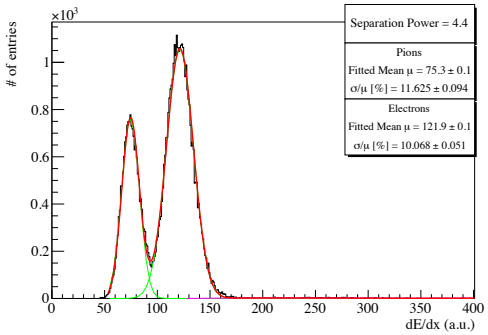

(b) 70 % HV scaling

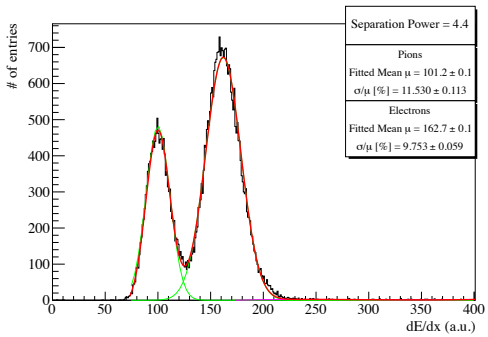

(c) 71 % HV scaling

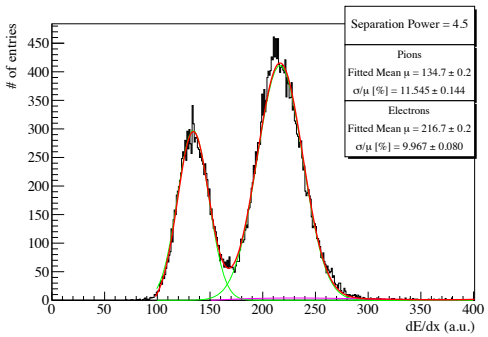

(d) 72 % HV scaling

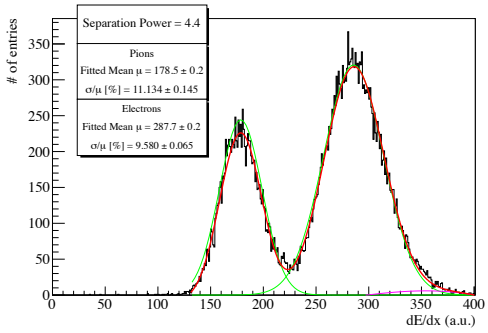

(e) 73 % HV scaling

Figure 4.23: Energy loss spectra for standard HV settings, 1 GeV/c (-) beam momentum with the truncations [5,25].

4.4 Comparision of the data with the PAI model predicion

The energy resolution prediction of the PAI model given by equation 2.16 depends on the number of dE/dx samples entering the calculation of the truncated mean. To verify the prediction with the measured data, the reconstructed tracks of run 681 were artificially shortened, simulating a smaller detector providing less samples. The prediction was calculated with the pressure in the PS East Area experimental hall $P = 950\,\text{hPa}$ and a sample size of $\Delta x = 0.75\,\text{cm}$. In figure 4.24 the energy resolution for electrons and pions is shown with the prediction of the energy resolution given by the PAI model. The relative resolution measured in the experiment is larger than the prediction but the data is in good agreement with the $n^{-0.43}$ dependency of the prediction. The energy resolution of pions is worse than the energy resolution of electrons, perhaps due to the different interaction of pions compared to electrons.

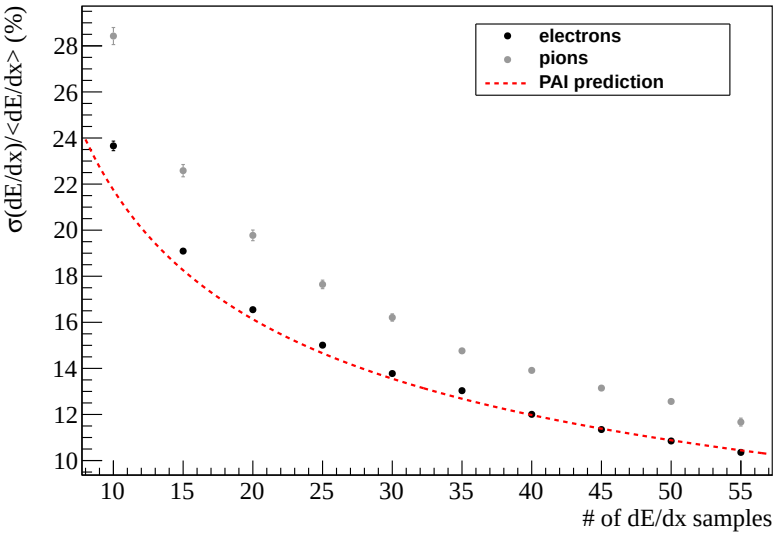

Figure 4.24: Energy resolution for different number of dE/dx samples taken from run 681

4.5 Results and comparision with the Tübingen analysis

The values for the relative resolution and the separation power were obtained for runs with beam momenta of 1 GeV/c, 2 GeV/c, 3 GeV/c and 6 GeV/c. The results for the runs with beam momentum 1 GeV and negative beam polarity are shown in figure 4.25 for the respective gain of the HV settings and the value of TF 2 in case of IBF settings. The results for the same settings with positive beam polarity are shown in figure 4.26 and 4.27. For IBF HV settings with positive beam polarity and momentum of 1 GeV no data was avaliable.

In the analysis of University of Tübingen the dE/dx samples of a track were obtained by calculating the truncated mean of the clusters' amplitude. The stepsize $\Delta x = 0.75\,\text{cm}$ was assumed to be constant. To compare the results of this analysis to those of University of Tübingen, one has to multiply the values of $\langle dE/dx \rangle$ obtained in this analysis by the factor of 0.75 to get the same scale.

The mean energy loss differs for different HV settings, because the arbitrary units depend on the gas amplification gain. The mean energy loss of the particle in gain adjusted units is expected to be constant for fixed momentum. In further beam times it could be investigated, if the energy loss is constant in gain adjusted units. A proper gain callibration is needed, which was not done for this test run.

The dependency of the electron resolution on the HV scaling factor for standard settings shows the same behaviour as in the Tübingen analysis. The electron energy resolution for different settings could be reproduced. The obtained value for the resolution for TF2 = 200 V/cm and a HV scaling factor of 100 % is 2 % worse than in the analysis of Tübingen. The different treatment of runs with low gas amplification in the analysis of Tübingen by reducing the cuts explains this disagreement. The calculated resolution for TF2 = 600 V/cm and a HV scaling factor of 107 % should be taken with caution and has a higher uncertainty. A trip occured during the run resulting in less data.

While the resolution for electrons is in agreement with the analysis of Tübingen, for pions a 1 % worse resolution was obtained in this analysis.

In figure 4.27 the pion energy resolution for a positive beam polarity and a HV scaling factor of 73 % deviates 2 % from the other values. This is caused by a second peak in the pion energy loss spectrum that biased the fit. The energy loss spectrum of particles, that deposited a signal below 150 in the Čherenkov counter, is shown in figure 4.29. Since the energy loss of pions and muons is comparable, the second peak could be attributed to muons contaminating the beam.

The separation power is shown in figure 4.28 for p =1 GeV/c, 2 GeV/c, 3 GeV/c and 6 GeV/c. The obtained values for beam momenta of 1 GeV/c and 2 GeV/c agree with the analysis of University of Tübingen, but the results for 3 GeV/c are not as expected. One would expect the separation power of pions and electrons to become smaller for larger momenta. The mean energy loss of pions approaches the mean

energy loss of electrons because of the beginning relativistic rise of pion mean energy loss, which can be seen in figure 2.1.

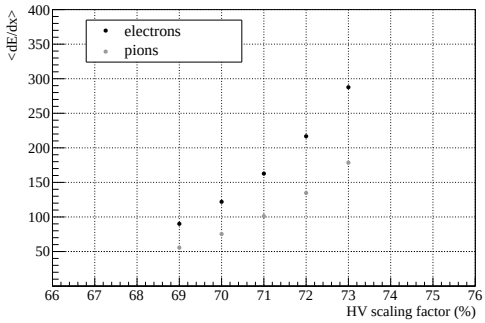

(a) $\langle dE/dx \rangle$, standard HV settings

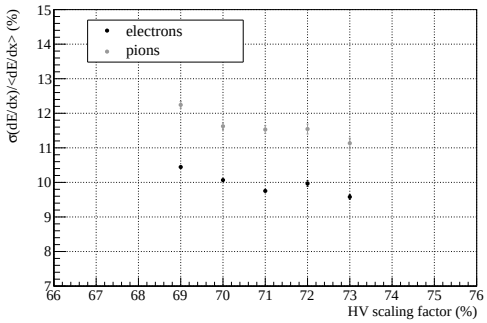

(b) $\sigma(dE/dx)$, standard HV settings

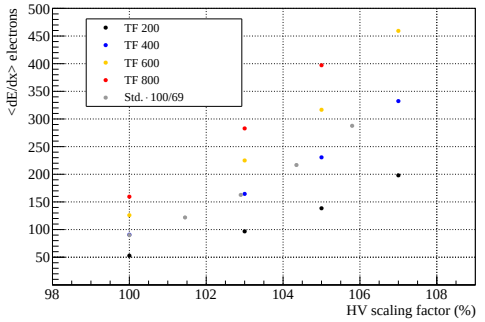

(c) $\langle dE/dx \rangle^e$, IBF HV settings

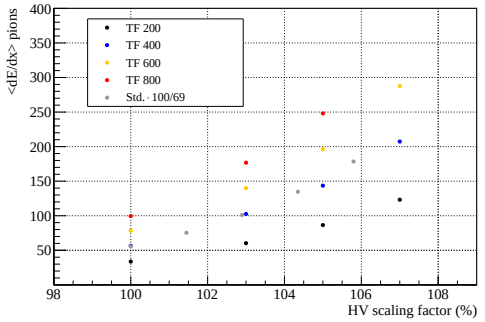

(d) $\langle dE/dx \rangle^\pi$, IBF HV settings

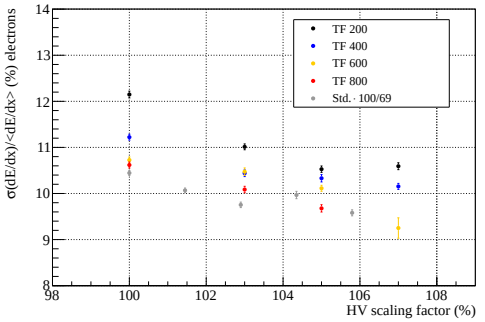

(e) $\sigma(dE/dx)^e$, IBF HV settings

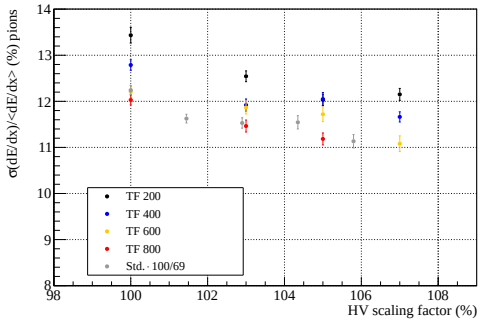

(f) $\sigma(dE/dx)^\pi$, IBF HV settings

Figure 4.25: Mean energy loss $\langle dE/dx \rangle$ (a.u.) and relative resolution $\sigma(dE/dx)$ for standard and IBF HV settings, beam momentum $p = 1\,\mathrm{GeV/c}$ and negative beam polarity with the truncations [5,25].

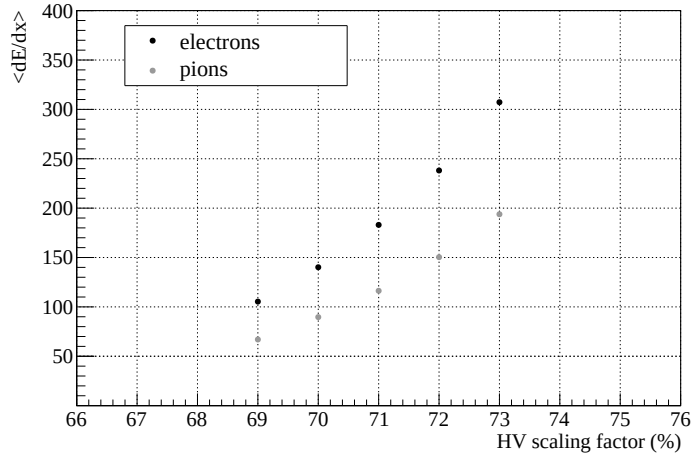

Figure 4.26: $\langle dE/dx \rangle$ for standard settings, beam momentum $p = 1\,\mathrm{GeV/c}$ and positive beam polarity

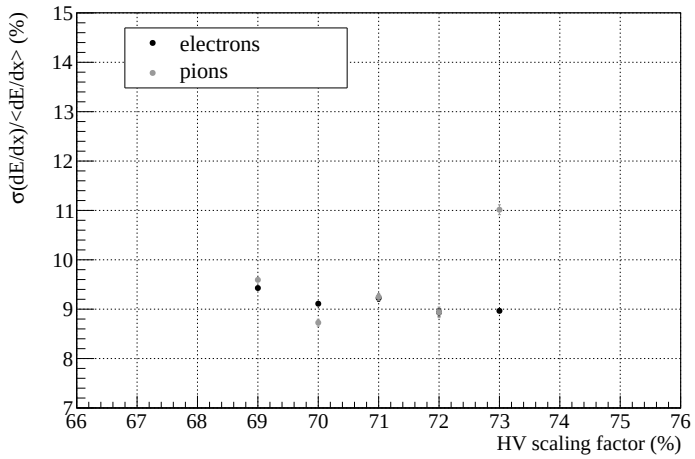

Figure 4.27: $\sigma(dE/dx)$ for standard settings, beam momentum $p = 1\,\mathrm{GeV/c}$ and positive beam polarity

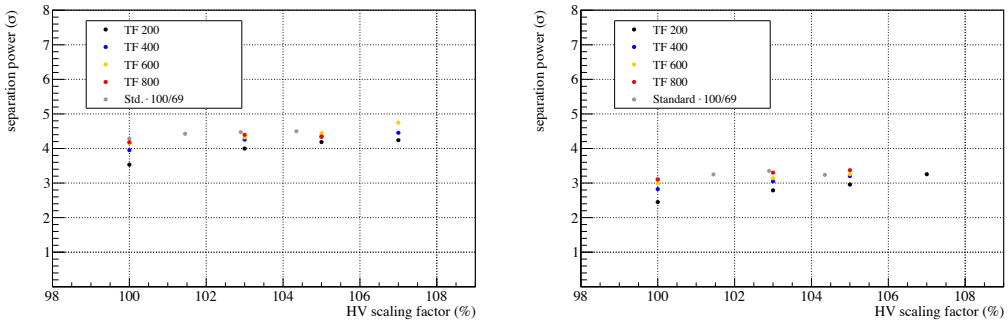

(a) $p = 1\,\mathrm{GeV/c}$, (-)

(b) $p = 2\,\mathrm{GeV/c}$, (-)

(c) $p = 3\,\mathrm{GeV/c}$, (-)

(d) $p = 6\,\mathrm{GeV/c}$, (+)

Figure 4.28: Separation power (σ) for standard and IBF HV settings with the truncations [5,25].

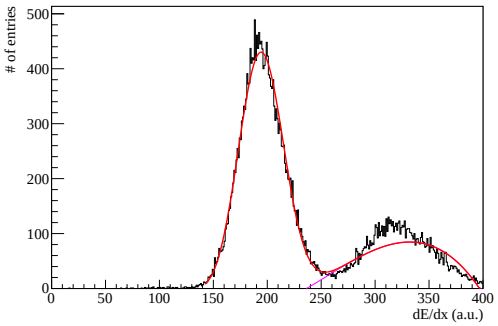

Figure 4.29: Energy loss spectrum for run 862, with Čherenkov counter cut < 150

Chapter 5

Conclusions and Outlook

A good energy loss resolution is crucial for reliable PID. The GEM based ALICE TPC has to provide a comparable energy loss resolution to the MWPCs used before the upgrade. In this thesis the energy loss resolution and the separation power of an IROC prototype equipped with GEMs has been investigated. With the fopiroot framework, tracks could be reconstructed from the ADC samples measured at the PS. A dE/dx task designed for the geometry of the IROC prototype has been created to generate dE/dx samples from tracks. Macros to determine the quality of the track reconstruction and to analyze the dE/dx samples were written. By automatization of the relevant analysis macros, a different set of parameters can be conveniently tested in a further analysis.

From the track parameters, an estimate for the position resolution was calculated to be 300 µm to 400 µm in y- and 550 µm to 600 µm in z-direction.

The energy loss resolution of the ALICE IROC prototype for different HV settings was in the interval 9 % to 11 % for electrons and in the interval 11 % to 14 % for pions. The results for the separation power between electrons and pions were spread around 4 σ for a beam momentum of 1 GeV/c and around 3 σ for a beam momentum of 2 GeV/c. The obtained values agreed for a beam momentum of with a previous analysis of the data by Jens Wiechula and Martin Ljunggren [36]. Open questions remain, though: The dependency of energy loss measurements from the HV settings should be investigated, for instance by calculating the energy loss in gain-adjusted units. It should be clarified, whether this effect originates from the data analysis or from the hardware. The analysis could be improved by creating a better gain map. In the Tübingen analysis application of the gain map improved the resolution by 0.5 % [36]. Nevertheless the gain correction failed for some pad rows. By creating a gain map with a test source like Krypton, a better gain correction could be applied. Unfortunately the detector was damaged in a subsequent run, so a gain map of the prototype for the same conditions as in the beamtime cannot be measured. Otherwise the pad rows, for which the gain correction failed, could be excluded in the analysis, which would result in dE/dx less samples but in a better gain correction. The energy loss resolution could be further improved with a optimal set of truncations.

The analysis of different truncations has shown, that further work is necessary to determine an optimal set of truncations for the final HV settings.

Instead of the primitive fitting of a Gaussian to the energy loss spectra, a convolution of a Gaussian and a exponential decay function could be used to fit the energy loss spectra more appropriately. This fitting method was used for the energy loss measurements with data of the FOPI-TPC [16].

In the scope of this thesis only energy spectra of runs with beam momentum of 1 GeV/c were discussed, however the tools to further investigate the data were created and all 84 runs were processed, ready to be discussed.

Appendix A

List of runs during beam time

run number	momentum (GeV/c)	polarity	HV scaling factor (%)	TF2 (V/cm)	remarks
680	1	-	69	3730	problem with file
681	1	-	69	3730	
682	1	-	70	3730	
683	1	-	71	3730	
684	1	-	72	3730	
685	1	-	73	3730	
686	1	-	100	200	
687	1	-	100	400	
688	1	-	100	600	
690	1	-	100	800	
691	1	-	103	200	
692	1	-	103	400	
693	1	-	103	600	
694	1	-	103	800	
698	1	-	105	200	
699	1	-	105	400	
700	1	-	105	600	
702	1	-	105	800	
703	1	-	107	200	
704	1	-	107	400	
705	1	-	107	600	trip, problem with file
706	1	-	107	600	trip
709	1	-	107	600	trip
713	2	-	100	200	
714	2	-	100	400	
715	2	-	100	600	
716	2	-	100	800	
717	2	-	103	200	

run number	momentum (GeV/c)	polarity	HV scaling factor (%)	TF2 (V/cm)	remarks
718	2	-	103	400	
719	2	-	103	600	
720	2	-	103	800	DAQ stuck
723	2	-	103	800	
724	2	-	105	200	DAQ stuck
726	2	-	105	200	
727	2	-	103	800	recheck settings
731	2	-	105	400	
733	2	-	105	600	
734	2	-	105	800	trip
735	2	-	105	800	
736	2	-	107	200	
737	2	-	107	400	trip
739	2	-	107	400	busy error
740	2	-	107	400	busy error
768	2	-	69	3730	
769	2	-	70	3730	
770	2	-	71	3730	
771	2	-	72	3730	
773	2	-	73	3730	
777	2	-	73	3730	
783	2	-	73	3730	
795	3	-	69	3730	
816	3	-	70	3730	
817	3	-	71	3730	
818	3	-	100	400	
820	3	-	100	600	trip
829	3	-	100	600	
830	3	-	103	200	
831	3	-	103	400	
832	3	-	105	200	
834	3	-	107	200	
838	3	-	105	400	
841	3	-	103	600	
842	3	-	100	800	

run number	momentum (GeV/c)	polarity	HV scaling factor (%)	TF2 (V/cm)	remarks
851	1	+	69	3730	
856	1	+	69	3730	
858	1	+	69	3730	
859	1	+	70	3730	
860	1	+	71	3730	
861	1	+	72	3730	
862	1	+	73	3730	
867	6	+	69	3730	
868	6	+	70	3730	
869	6	+	71	3730	
870	6	+	72	3730	DAQ stuck
871	6	+	72	3730	
872	6	+	73	3730	
873	6	+	100	400	
876	6	+	103	200	
879	6	+	105	200	
881	6	+	107	200	
882	6	+	103	400	
883	6	+	105	400	
884	6	+	100	600	
886	6	+	103	600	
887	6	+	100	800	
889	1	-	100	200	
891	1	-	103	200	
892	1	-	105	200	
893	1	-	100	400	busy error
896	1	-	100	400	
897	1	-	107	200	
898	1	-	103	400	
899	1	-	105	400	
900	1	-	100	200	

The dE/dx samples of the runs 851, 856 and 858 were merged in the analysis, since the runs had the same settings. The same was done for the dE/dx samples of the runs 773, 777 and 783. Runs with trips (with exception of run 709), DAQ errors and incorrectly merged files were not considered in this analysis.

Appendix B

Results of the analysis for higher beam momenta

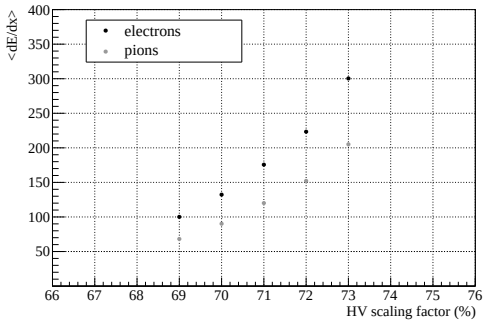

(a) $\langle dE/dx \rangle$, standard HV settings

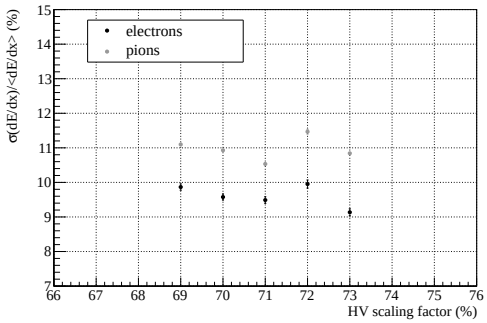

(b) $\sigma(dE/dx)$, standard HV settings

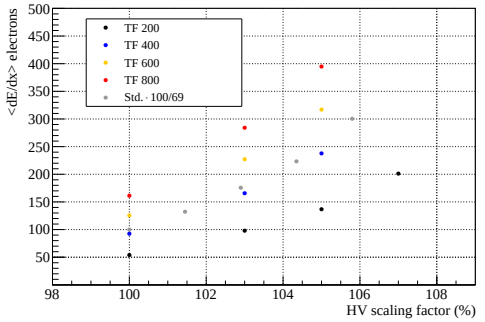

(c) $\langle dE/dx \rangle^e$, IBF HV settings

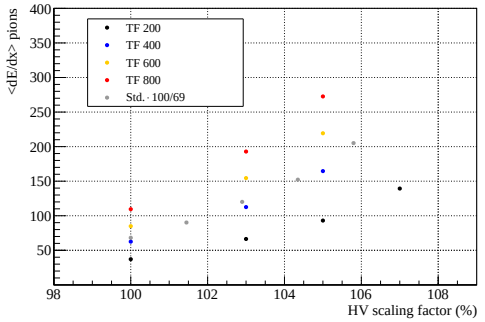

(d) $\langle dE/dx \rangle^\pi$, IBF HV settings

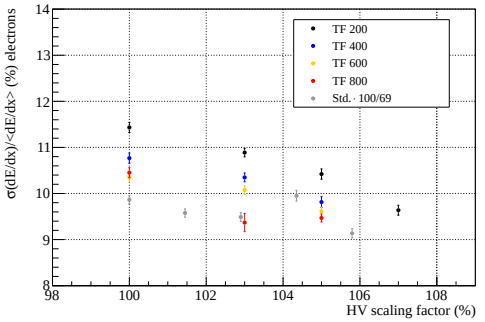

(e) $\sigma(dE/dx)^e$, IBF HV settings

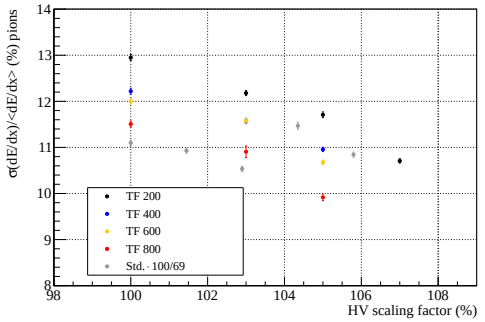

(f) $\sigma(dE/dx)^\pi$, IBF HV settings

Figure B.1: Mean energy loss $\langle dE/dx \rangle$ and relative resolution $\sigma(dE/dx)$ for standard and IBF HV settings, beam momentum $p = 2\,\mathrm{GeV/c}$ and negative beam polarity with the truncations [5,25].

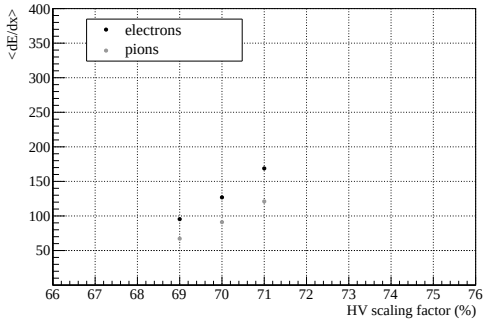

(a) $\langle dE/dx \rangle$, standard HV settings

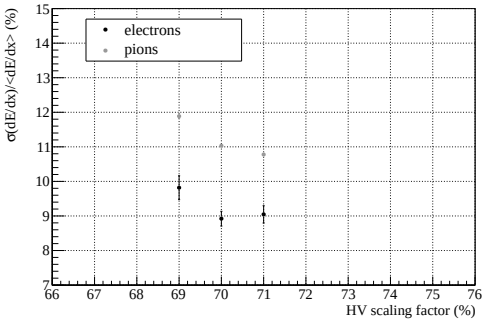

(b) $\sigma(dE/dx)$, standard HV settings

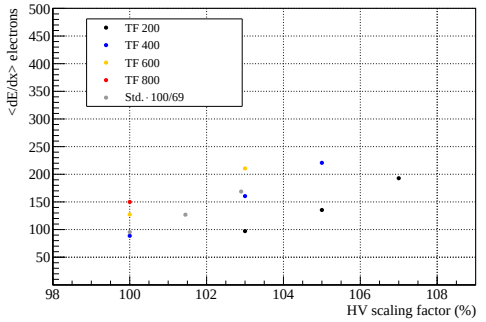

(c) $\langle dE/dx \rangle^e$, IBF HV settings

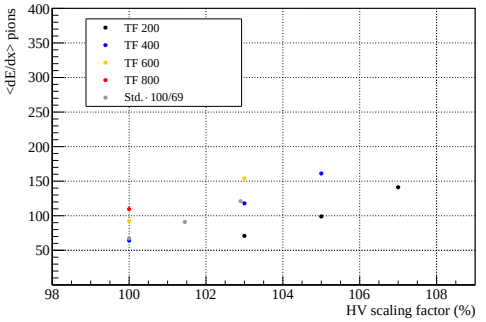

(d) $\langle dE/dx \rangle^\pi$, IBF HV settings

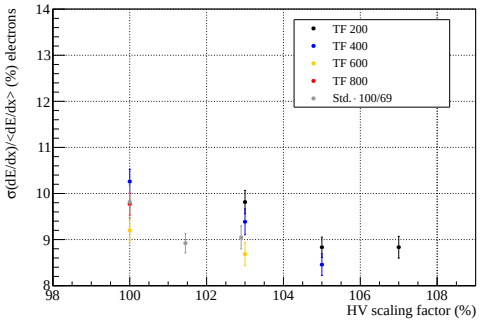

(e) $\sigma(dE/dx)^e$, IBF HV settings

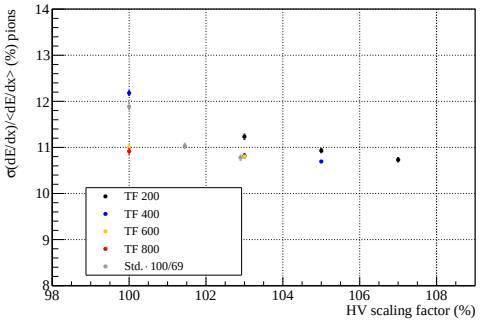

(f) $\sigma(dE/dx)^\pi$, IBF HV settings

Figure B.2: Mean energy loss $\langle dE/dx \rangle$ and relative resolution $\sigma(dE/dx)$ for standard and IBF HV settings, beam momentum $p = 3\,\mathrm{GeV/c}$ and negative beam polarity with the truncations [5,25].

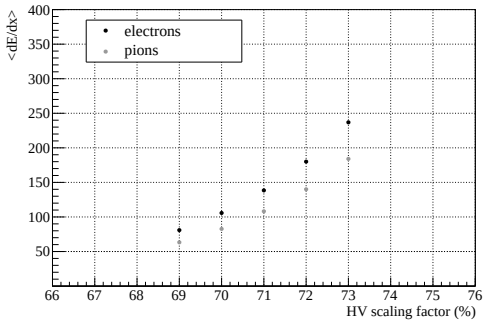

(a) $\langle dE/dx \rangle$, standard HV settings

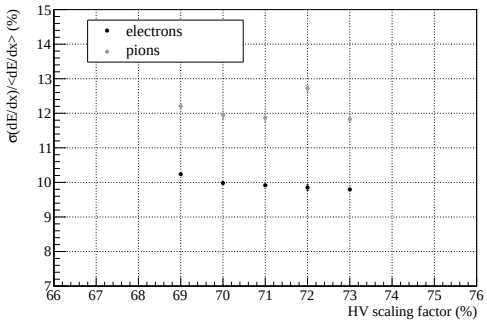

(b) $\sigma(dE/dx)$, standard HV settings

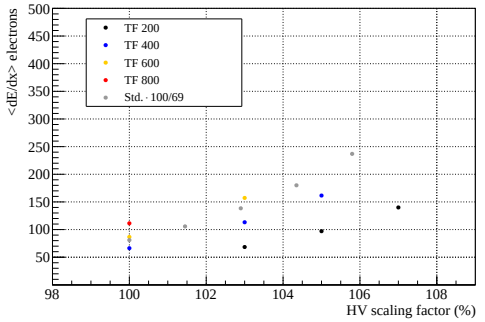

(c) $\langle dE/dx \rangle^e$, IBF HV settings

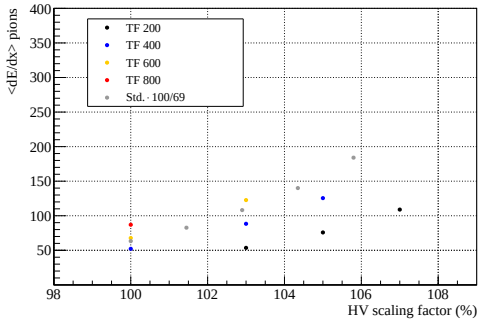

(d) $\langle dE/dx \rangle^\pi$, IBF HV settings

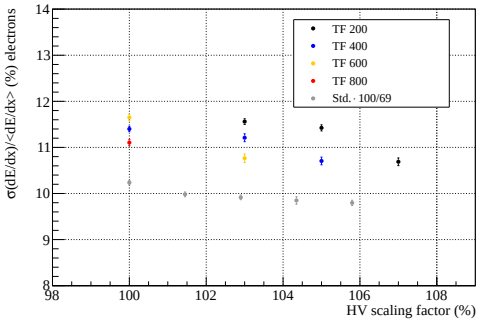

(e) $\sigma(dE/dx)^e$, IBF HV settings

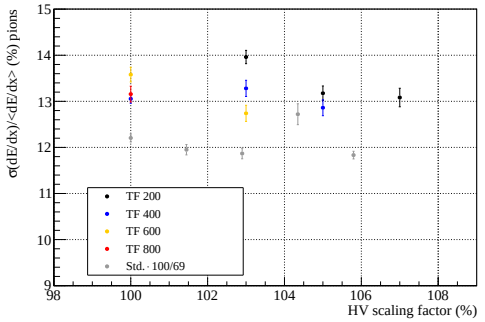

(f) $\sigma(dE/dx)^\pi$, IBF HV settings

Figure B.3: Mean energy loss $\langle dE/dx \rangle$ and relative resolution $\sigma(dE/dx)$ for standard and IBF HV settings, beam momentum $p = 6\,\mathrm{GeV/c}$ and positive beam polarity with the truncations [5,25].

Appendix C

Acknowledgements

I want to express my deepest gratitude to Prof. Laura Fabbietti for making this thesis possible. It was very exciting to work with data from a particle physics experiment connected to the LHC and to learn about the reconstruction of particle tracks from simple ADC signals. Despite her busy schedule she took her time to give me suggestions for my work and asked questions that focused me on the physics behind the data analysis.

My sincerest thanks go out to Dr. Bernhard Ketzer who not only thaught me a lot about particle detection and the underlying physics in his lecture on particle detectors but also encouraged me and gave many helpful suggestions for my work. Regarding his inspiring motivation and deep knowledge of experimental physics, I am very grateful for his involvement in my work.

Laura and Bernhard established a great working group. I would like to thank the people at E18 where I worked: I want to thank Johannes Rauch for the well-documented code and for his advise on finding the best parameters for the Riemann Pattern recognition. He is not only a gifted programmer and great guy, but also a great musician at the keyboard. Felix Böhmer and Stefan Huber gave helpful advice on coding and especially Felix is an expert for programming languages. I would like to thank Jens Wiechula for answering my questions regarding his analysis.

I want to thank Sverre Dørheim for advising me during my thesis. In the beginning he took a lot of his time to help me with the Linux enviroment, the framework and ROOT, since I started the thesis with very limited knowledge of data analysis and started to learn C++ programming only a few months before the beginning of my thesis. By asking questions he helped me to break more than one mental block and his encouragement and friendly spirit helped me over many unexpected problems with programming. Sverre, I wish you and your girlfriend all the best! Thank you for advising me, I learned a lot (not only about physics) and enjoyed being your roommate.

I would like to thank Andreas Mathis, Christopher Bilko and Jacopo Margutti, with whom I had the privilege to experience shifts in the beam time for Andreas' bachelor thesis. It was exciting to see, how data is taken in a particle physics experiment. I would also like to thank Robert Glas, Julia Stadler, Andreas Mathis and

Stefan Wallner for the good times we shared in programming classes and during my thesis and for their advice.

Special thanks go out to Christopher Mittag and Wolfgang Neumeier for their advice on writing and on making computer graphics.

I want to thank my parents for supporting me in my courses of study. Without your support and love I would not have been able to write these lines.

Bibliography

[1] Ackermann, K. H. ; Bieser, F. ; Brady, F. P. ; Cebra, D. ; Draper, J. E. ; Eckardt, V. ; Eggert, T. ; Fessler, H. ; Foley, K. J. ; Ghazikhanian, V. ; Hallman, T. J. ; Heffner, M. ; Hummler, H. ; Klay, J. ; Klein, S. R. ; Lebedev, A. ; LeVine, M. J. ; Ljubicic, T. ; Curto, G. L. ; Longacre, R. S. ; Oldenburg, M. ; Ritter, H. ; Romero, J. L. ; Schmitz, N. ; Schuttauf, A. ; Seyboth, J. ; Seyboth, P. ; Vidal, M. ; Whitten, C. ; Yamamoto, E.: The forward time projection chamber in STAR. In: *Nuclear Instruments and Methods in Physics Research A* 499 (2003), März, S. 713–719. `http://dx.doi.org/10.1016/S0168-9002(02)01968-X`. – DOI 10.1016/S0168–9002(02)01968–X

[2] Afanasev, S. u. a.: The NA49 large acceptance hadron detector. In: *Nucl.Instrum.Meth.* A430 (1999), S. 210–244. `http://dx.doi.org/10.1016/S0168-9002(99)00239-9`. – DOI 10.1016/S0168–9002(99)00239–9

[3] Aihara, H. ; Alston-Garnjost, M. ; Badtke, D. H. ; Bakken, J. A. ; Barbaro-Galtieri, A. ; Barnes, A. V. ; Barnett, B. A. ; Blumenfeld, B. ; Bross, A. ; Buchanan, C. D. ; Carithers, W. C. ; Chamberlain, O. ; Chiba, J. ; Chien, C.-Y. ; Clark, A. R. ; Dahl, O. I. ; Day, C. T. ; Delpierre, P. ; Derby, K. A. ; Eberhard, P. H. ; Fancher, D. L. ; Fujii, H. ; Fujii, T. ; Gabioud, B. ; Gary, J. W. ; Gorn, W. ; Hadley, N. J. ; Hauptman, J. M. ; Heck, B. ; Hilke, H. J. ; Huth, J. E. ; Hylen, J. ; Iwasaki, H. ; Kamae, T. ; Kenney, R. W. ; Kerth, L. T. ; Koda, R. ; Kofler, R. R. ; Kwong, K. K. ; Layter, J. G. ; Lindsey, C. S. ; Loken, S. C. ; Lu, X.-Q. ; Lynch, G. R. ; Madansky, L. ; Madaras, R. J. ; Majka, R. ; Mallet, J. ; Martin, P. S. ; Maruyama, K. ; Marx, J. N. ; Matthews, J. A. J. ; Melnikoff, S. O. ; Moses, W. ; Nemethy, P. ; Nygren, D. R. ; Oddone, P. J. ; Park, D. ; Pevsner, A. ; Pripstein, M. ; Robrish, P. R. ; Ronan, M. T. ; Ross, R. R. ; Rouse, F. R. ; Shapiro, G. ; Shapiro, M. D. ; Shen, B. C. ; Slater, W. E. ; Stevenson, M. L. ; Stork, D. H. ; Ticho, H. K. ; Toge, N. ; Urban, M. ; van Dalen, G. J. ; van Tyen, R. ; Videau, H. ; Wayne, M. ; Wenzel, W. A. ; Vandaalen Wetters, R. F. ; Yamauchi, M. ; Zeller, M. E. ; Zhang, W.-M. ; Madaras, R. J.: Spatial Resolution of the PEP-4 Time Projection Chamber. In: *IEEE Transactions on Nuclear Science* 30

(1983), S. 76–81. http://dx.doi.org/10.1109/TNS.1983.4332223. – DOI 10.1109/TNS.1983.4332223

[4] Al-Turany, M. ; Bertini, D. ; Karabowicz, R. ; Kresan, D. ; Malzacher, P. ; Stockmanns, T. ; Uhlig, F.: The FairRoot framework. In: *Journal of Physics Conference Series* 396 (2012), Dezember, Nr. 2, S. 022001. http://dx.doi.org/10.1088/1742-6596/396/2/022001. – DOI 10.1088/1742–6596/396/2/022001

[5] ALICE Collaboration ; Aamodt, K. ; Abrahantes Quintana, A. ; Achenbach, R. ; Acounis, S. ; Adamová, D. ; Adler, C. ; Aggarwal, M. ; Agnese, F. ; Aglieri Rinella, G. ; al. et: The ALICE experiment at the CERN LHC. In: *Journal of Instrumentation* 3 (2008), August, S. 8002. http://dx.doi.org/10.1088/1748-0221/3/08/S08002. – DOI 10.1088/1748–0221/3/08/S08002

[6] Allison, W.W.M. ; Cobb, J.H.: Relativistic Charged Particle Identification by Energy Loss. In: *Ann.Rev.Nucl.Part.Sci.* 30 (1980), S. 253–298

[7] Alme, J. ; Andres, Y. ; Appelshäuser, H. ; Bablok, S. ; Bialas, N. ; Bolgen, R. ; Bonnes, U. ; Bramm, R. ; Braun-Munzinger, P. ; Campagnolo, R. ; Christiansen, P. ; Dobrin, A. ; Engster, C. ; Fehlker, D. ; Foka, Y. ; Frankenfeld, U. ; Gaardhøje, J. J. ; Garabatos, C. ; Glässel, P. ; Gonzalez Gutierrez, C. ; Gros, P. ; Gustafsson, H.-A. ; Helstrup, H. ; Hoch, M. ; Ivanov, M. ; Janik, R. ; Junique, A. ; Kalweit, A. ; Keidel, R. ; Kniege, S. ; Kowalski, M. ; Larsen, D. T. ; Lesenechal, Y. ; Lenoir, P. ; Lindegaard, N. ; Lippmann, C. ; Mager, M. ; Mast, M. ; Matyja, A. ; Munkejord, M. ; Musa, L. ; Nielsen, B. S. ; Nikolic, V. ; Oeschler, H. ; Olsen, E. K. ; Oskarsson, A. ; Osterman, L. ; Pikna, M. ; Rehman, A. ; Renault, G. ; Renfordt, R. ; Rossegger, S. ; Röhrich, D. ; Røed, K. ; Richter, M. ; Rueshmann, G. ; Rybicki, A. ; Sann, H. ; Schmidt, H.-R. ; Siska, M. ; Sitár, B. ; Soegaard, C. ; Soltveit, H.-K. ; Soyk, D. ; Stachel, J. ; Stelzer, H. ; Stenlund, E. ; Stock, R. ; Strmeň, P. ; Szarka, I. ; Ullaland, K. ; Vranic, D. ; Veenhof, R. ; Westergaard, J. ; Wiechula, J. ; Windelband, B.: The ALICE TPC, a large 3-dimensional tracking device with fast readout for ultra-high multiplicity events. In: *Nuclear Instruments and Methods in Physics Research A* 622 (2010), Oktober, S. 316–367. http://dx.doi.org/10.1016/j.nima.2010.04.042. – DOI 10.1016/j.nima.2010.04.042

[8] Anderson, M. ; Berkovitz, J. ; Betts, W. ; Bossingham, R. ; Bieser, F. ; Brown, R. ; Burks, M. ; Calderon de la Barca Sanchez, M. ; Cebra, D. ; Cherney, M. ; Chrin, J. ; Edwards, W. R. ; Ghazikhanian,

V. ; Greiner, D. ; Gilkes, M. ; Hardtke, D. ; Harper, G. ; Hjort, E. ; Huang, H. ; Igo, G. ; Jacobson, S. ; Keane, D. ; Klein, S. R. ; Koehler, G. ; Kotchenda, L. ; Lasiuk, B. ; Lebedev, A. ; Lin, J. ; Lisa, M. ; Matis, H. S. ; Nystrand, J. ; Panitkin, S. ; Reichold, D. ; Retiere, F. ; Sakrejda, I. ; Schweda, K. ; Shuman, D. ; Snellings, R. ; Stone, N. ; Stringfellow, B. ; Thomas, J. H. ; Trainor, T. ; Trentalange, S. ; Wells, R. ; Whitten, C. ; Wieman, H. ; Yamamoto, E. ; Zhang, W.: The STAR time projection chamber: a unique tool for studying high multiplicity events at RHIC. In: *Nuclear Instruments and Methods in Physics Research A* 499 (2003), März, S. 659–678. `http://dx.doi.org/10.1016/S0168-9002(02)01964-2`. – DOI 10.1016/S0168–9002(02)01964–2

[9] Atwood, W B. ; Barczewski, T ; Bauerdick, L A T. ; Bellantoni, L ; Blucher, E ; Blum, Walter ; Boudreau, J F. ; Boyle, O ; Cinabro, D ; Conway, J S. ; Cowan, G D. ; Cowen, D F. ; Efthymiopoulos, I ; Faure, P ; Feng, Z ; Fidecaro, F ; Gobbo, B ; Halley, A W. ; Haywood, S ; Jahn, A ; Jared, R C. ; Johnson, R P. ; Kasemann, M ; Kleinknecht, K ; LeClaire, B ; Lehraus, Ivan ; Löfstedt, B ; Lohse, T ; Lüke, D ; Lusiani, A ; Marrocchesi, P S. ; May, J ; Meyer, T C. ; Morsani, F ; Minten, Adolf G. ; Pater, J R. ; Pollmann, D ; Price, M ; Richter, R H. ; Richter, W ; Roehn, S ; Rolandi, Luigi ; Roth, A E. ; Rotscheidt, Herbert ; Schlatter, W D. ; Schmelling, M ; Schmidt, H ; Schröder, J ; Settles, Ronald ; Steeg, F ; Stefanini, G ; Stierlin, U ; Takashima, M ; Tejessy, W ; Have, I ten ; Thomas, J ; Vayaki, Anna ; Wear, J ; Wiedenmann, W ; Witzeling, W ; Lan, Wu S.: Performance of the ALEPH Time Projection Chamber. In: *Nucl. Instrum. Methods Phys. Res., A* 306 (1991), Feb, Nr. CERN-PPE-91-24. CERN-ALEPH-PUB-91-047, S. 446–458. 36 p

[10] Berger, Martin: A GEM-TPC detector for FOPI and PANDA. In: *PoS* BORMIO2011 (2011), S. 020

[11] Beringer, J. ; Arguin, J. F. ; Barnett, R. M. ; Copic, K. ; Dahl, O. ; Groom, D. E. ; Lin, C. J. ; Lys, J. ; Murayama, H. ; Wohl, C. G. ; Yao, W. M. ; Zyla, P. A. ; Amsler, C. ; Antonelli, M. ; Asner, D. M. ; Baer, H. ; Band, H. R. ; Basaglia, T. ; Bauer, C. W. ; Beatty, J. J. ; Belousov, V. I. ; Bergren, E. ; Bernardi, G. ; Bertl, W. ; Bethke, S. ; Bichsel, H. ; Biebel, O. ; Blucher, E. ; Blusk, S. ; Brooijmans, G. ; Buchmueller, O. ; Cahn, R. N. ; Carena, M. ; Ceccucci, A. ; Chakraborty, D. ; Chen, M. C. ; Chivukula, R. S. ; Cowan, G. ; D'Ambrosio, G. ; Damour, T. ; Florian, D. de ; Gouvêa, A. de ; DeGrand, T. ; Jong, P. de ; Dissertori, G. ; Dobrescu, B. ; Doser, M. ; Drees, M. ; Edwards, D. A. ; Eidelman, S. ; Erler, J. ; Ezhela, V. V. ; Fetscher, W. ; Fields, B. D. ; Foster, B. ;

Gaisser, T. K. ; Garren, L. ; Gerber, H. J. ; Gerbier, G. ; Gherghetta, T. ; Golwala, S. ; Goodman, M. ; Grab, C. ; Gritsan, A. V. ; Grivaz, J. F. ; Grünewald, M. ; Gurtu, A. ; Gutsche, T. ; Haber, H. E. ; Hagiwara, K. ; Hagmann, C. ; Hanhart, C. ; Hashimoto, S. ; Hayes, K. G. ; Heffner, M. ; Heltsley, B. ; Hernández-Rey, J. J. ; Hikasa, K. ; Höcker, A. ; Holder, J. ; Holtkamp, A. ; Huston, J. ; Jackson, J. D. ; Johnson, K. F. ; Junk, T. ; Karlen, D. ; Kirkby, D. ; Klein, S. R. ; Klempt, E. ; Kowalewski, R. V. ; Krauss, F. ; Kreps, M. ; Krusche, B. ; Kuyanov, Yu. V. ; Kwon, Y. ; Lahav, O. ; Laiho, J. ; Langacker, P. ; Liddle, A. ; Ligeti, Z. ; Liss, T. M. ; Littenberg, L. ; Lugovsky, K. S. ; Lugovsky, S. B. ; Mannel, T. ; Manohar, A. V. ; Marciano, W. J. ; Martin, A. D. ; Masoni, A. ; Matthews, J. ; Milstead, D. ; Miquel, R. ; Mönig, K. ; Moortgat, F. ; Nakamura, K. ; Narain, M. ; Nason, P. ; Navas, S. ; Neubert, M. ; Nevski, P. ; Nir, Y. ; Olive, K. A. ; Pape, L. ; Parsons, J. ; Patrignani, C. ; Peacock, J. A. ; Petcov, S. T. ; Piepke, A. ; Pomarol, A. ; Punzi, G. ; Quadt, A. ; Raby, S. ; Raffelt, G. ; Ratcliff, B. N. ; Richardson, P. ; Roesler, S. ; Rolli, S. ; Romaniouk, A. ; Rosenberg, L. J. ; Rosner, J. L. ; Sachrajda, C. T. ; Sakai, Y. ; Salam, G. P. ; Sarkar, S. ; Sauli, F. ; Schneider, O. ; Scholberg, K. ; Scott, D. ; Seligman, W. G. ; Shaevitz, M. H. ; Sharpe, S. R. ; Silari, M. ; Sjöstrand, T. ; Skands, P. ; Smith, J. G. ; Smoot, G. F. ; Spanier, S. ; Spieler, H. ; Stahl, A. ; Stanev, T. ; Stone, S. L. ; Sumiyoshi, T. ; Syphers, M. J. ; Takahashi, F. ; Tanabashi, M. ; Terning, J. ; Titov, M. ; Tkachenko, N. P. ; Törnqvist, N. A. ; Tovey, D. ; Valencia, G. ; Bibber, K. van ; Venanzoni, G. ; Vincter, M. G. ; Vogel, P. ; Vogt, A. ; Walkowiak, W. ; Walter, C. W. ; Ward, D. R. ; Watari, T. ; Weiglein, G. ; Weinberg, E. J. ; Wiencke, L. R. ; Wolfenstein, L. ; Womersley, J. ; Woody, C. L. ; Workman, R. L. ; Yamamoto, A. ; Zeller, G. P. ; Zenin, O. V. ; Zhang, J. ; Zhu, R. Y. ; Harper, G. ; Lugovsky, V. S. ; Schaffner, P.: Review of Particle Physics. In: *Phys. Rev. D* 86 (2012), Jul, 010001. `http://dx.doi.org/10.1103/PhysRevD.86.010001`. – DOI 10.1103/PhysRevD.86.010001

[12] Bethe, H.: Zur Theorie des Durchgangs schneller Korpuskularstrahlen durch Materie. In: *Annalen der Physik* 397 (1930), S. 325–400. `http://dx.doi.org/10.1002/andp.19303970303`. – DOI 10.1002/andp.19303970303

[13] Bichsel, H.: A method to improve tracking and particle identification in TPCs and silicon detectors. In: *Nucl.Instrum.Meth.* A562 (2006), S. 154–197. `http://dx.doi.org/10.1016/j.nima.2006.03.009`. – DOI 10.1016/j.nima.2006.03.009

[14] Bichsel, Hans ; Saxon, Roberta P.: Comparison of calculational methods for

straggling in thin absorbers. In: *Phys. Rev. A* 11 (1975), Apr, 1286–1296. http://dx.doi.org/10.1103/PhysRevA.11.1286. – DOI 10.1103/PhysRevA.11.1286

[15] Blum, Walter ; Riegler, Werner ; Rolandi, Luigi: *Particle Detection with drift Chambers*. 2nd ed. Berlin : Springer, 2008

[16] Böhmer, Felix V.: *First Measurement of dE/dx with a large GEM-based TPC*. – submitted to Nuclear Instruments and Methods A

[17] Böhmer, Felix V.: *A High-Rate Time Projection Chamber for panda: Simulation Studies and GPU-based Track-Finding*, Technische Universität München, Diplomarbeit, 2009

[18] Brand, C. ; Cairanti, G. ; Charpentier, P. ; Clara, M.P. ; Delikaris, D. ; Foeth, H. ; Heck, B.W. ; Hilke, H.J. ; Sulkowski, K. ; Aubert, C. ; Billoir, P. ; Boutonnet, C. ; Courty, P. ; Crozon, M. ; Delpierre, P. ; Diaczek, A. ; Mas, J. ; Saget, G. ; Tilquin, A. ; Turlot, J.P. ; Vergezac, P. ; Antilogus, P. ; Augustin, J.E. ; Gaillard, M. ; Gros, M.H. ; Hrisoho, A. ; Jean-Marie, B. ; Lepeltier, V. ; Noppe, J.M. ; Richard, F. ; Truong, K. ; Bolognese, T. ; Borgeaud, P. ; DeBeer, M. ; Jarry, P. ; Mur, M. ; Raoul, J.C. ; Ruhlmann, V. ; Sacquin, Y. ; Siegrist, P. ; Smadja, G. ; Turluer, M. ; Vilanova, D. ; Darbo, G. ; Vernocchi, F. ; Barring, O. ; Jarlskog, G. ; Kack, S. ; Lorstadt, B. ; Mjornmark, U.: The DELPHI time projection chamber. In: *Nuclear Science, IEEE Transactions on* 36 (1989), Nr. 1, S. 122–126. http://dx.doi.org/10.1109/23.34417. – DOI 10.1109/23.34417. – ISSN 0018–9499

[19] Brun, R. ; Rademakers, F.: ROOT: An object oriented data analysis framework. In: *Nucl.Instrum.Meth.* A389 (1997), S. 81–86. http://dx.doi.org/10.1016/S0168-9002(97)00048-X. – DOI 10.1016/S0168–9002(97)00048–X

[20] Cardini, Alessandro ; Bencivenni, Giovanni ; De Simone, Patrizia: The Operational Experience of the Triple-GEM Detectors of the LHCb Muon System: Summary of 2 Years of Data Taking. (2012), Nov

[21] Friedrich, J ; Huber, S ; Ketzer, B ; Kramer, M ; Konorov, I ; Mann, A ; Paul, S: A digital calorimetric trigger for the COMPASS experiment at CERN. (2009)

[22] Garabatos, C.: The ALICE TPC. In: *Nuclear Instruments and Methods in Physics Research Section A: Accelerators, Spectrometers, Detectors and Associated Equipment* 535 (2004), 197 - 200. http://d

x.doi.org/ http:/ / dx.doi.org/ 10.1016/ j.nima.2004.07.127. – DOI http://dx.doi.org/10.1016/j.nima.2004.07.127. – ISSN 0168–9002

[23] Hoppner, C. ; Neubert, S. ; Ketzer, B. ; Paul, S.: A Novel Generic Framework for Track Fitting in Complex Detector Systems. In: *Nucl.Instrum.Meth.* A620 (2010), S. 518–525. http://dx.doi.org/10.1016/j.nima.2010.03.136. – DOI 10.1016/j.nima.2010.03.136

[24] Jönsson, L.: *Front end electronics for a TPC at future linear colliders.* http://www.eudet.org/e26/e28/e86887/e105928/EUDET-Memo-2010-30.pdf, November 2010

[25] Kalman, R. E.: A New Approach to Linear Filtering And Prediction Problems. In: *ASME Journal of Basic Engineering* (1960)

[26] Ketzer, B. ; Altunbas, M.C. ; Dehmelt, K. ; Ehlers, J. ; Friedrich, J. ; Grube, B. ; Kappler, S. ; Konorov, I. ; Paul, S. ; Placci, A. ; Ropelewski, L. ; Sauli, F. ; Schmitt, L. ; Simon, F.: Triple GEM tracking detectors for COMPASS. In: *Nuclear Science, IEEE Transactions on* 49 (2002), Nr. 5, S. 2403–2410. http://dx.doi.org/10.1109/TNS.2002.803891. – DOI 10.1109/TNS.2002.803891. – ISSN 0018–9499

[27] Landau, L.: On the energy loss of fast particles by ionization. In: *J.Phys.(USSR)* 8 (1944), S. 201–205

[28] Leo, William R.: *Techniques for Nuclear and Particle Physics Experiments: A How-to Approach.* 2., überarb. A. Springer, Berlin, 1994 http://www.amazon.com/exec/obidos/redirect?tag=citeulike07-20&path=ASIN/3540572805. – ISBN 3540572805

[29] Lippmann, C.: Particle identification. In: *Nuclear Instruments and Methods in Physics Research A* 666 (2012), Feb, S. 148–172. http://dx.doi.org/10.1016/j.nima.2011.03.009. – DOI 10.1016/j.nima.2011.03.009

[30] Ljunggren, Martin: *Residual studies of test beam data.* TPC upgrade meeting, 12 2012

[31] Musa, L: Upgrade Strategy for ALICE at High Rate / CERN. Geneva, Mar 2012 (CERN-LHCC-2012-004. LHCC-G-158). – Forschungsbericht

[32] Nygren, D.R. ; Marx, J.N.: The Time Projection Chamber. In: *Phys.Today* 31N10 (1978), S. 46–53

[33] Radiation Units, International C. ; Measurements: Average Energy Required to Produce an Ion Pair. In: *ICRU Report* 31 (1979)

[34] Rauch, Johannes: *Tracking with a High-Rate GEM-TPC*, Technische Universität München, Diplomarbeit, 2012

[35] Sauli, F.: GEM: A new concept for electron amplification in gas detectors. In: *Nuclear Instruments and Methods A* 386 (1997), Feb, Nr. 2-3, 531–534. ht tp://dx.doi.org/10.1016/s0168-9002(96)01172-2. – DOI 10.1016/s0168–9002(96)01172–2. – ISSN 01689002

[36] The ALICE TPC collaboration: *Technical Design Report of the ALICE TPC Upgrade*

[37] The TOTEM Collaboration ; Anelli, G ; Antchev, G ; Aspell, P ; Avati, V ; Bagliesi, M G. ; Berardi, V ; Berretti, M ; Boccone, V ; Bottigli, U ; Bozzo, M ; BrÃ¼cken, E ; Buzzo, A ; Cafagna, F ; Calicchio, M ; Capurro, F ; Catanesi, M G. ; Catastini, P L. ; Cecchi, R ; Cerchi, S ; Cereseto, R ; Ciocci, M A. ; Cuneo, S ; ViÃ, C D. ; David, E ; Deile, M ; Dimovasili, E ; Doubrava, M ; Eggert, K ; Eremin, V ; Ferro, F ; Foussat, A ; GaluÅ¡ka, M ; Garcia, F ; Gherarducci, F ; Giani, S ; Greco, V ; Hasi, J ; Haug, F ; Heino, J ; Hilden, T ; Jarron, P ; Joram, C ; Kalliopuska, J ; Kaplon, J ; KaÅ¡par, J ; KundrÃ¡t, V ; Kurvinen, K ; Lacroix, J M. ; Lami, S ; Latino, G ; Lauhakangas, R ; Lippmaa, E ; LokajÃ[U+008D]ek, M ; Vetere, M L. ; Rodriguez, F L. ; Macina, D ; MacrÃ, M ; MagazzÃ¹, C ; MagazzÃ¹, G ; Magri, A ; Maire, G ; Manco, A ; Meucci, M ; Minutoli, S ; Morelli, A ; Musico, P ; Negri, M ; Niewiadomski, H ; Noschis, E ; Notarnicola, G ; Oliveri, E ; Oljemark, F ; Orava, R ; Oriunno, M ; Perrot, A-L ; Ã[U+0096]sterberg, K ; Paoletti, R ; Pedreschi, E ; PetÃ¤jÃ¤rvi, J ; Pollovio, P ; Quinto, M ; Radermacher, E ; Radicioni, E ; Rangod, S ; Ravotti, F ; Rella, G ; Robutti, E ; Ropelewski, L ; Ruggiero, G ; Rummel, A ; Saarikko, H ; Sanguinetti, G ; Santroni, A ; Scribano, A ; Sette, G ; Snoeys, W ; Spinella, F ; Squillacioti, P ; Ster, A ; Taylor, C ; Tazzioli, A ; Torazza, D ; Trovato, A ; Trummal, A ; Turini, N ; Vacek, V ; Remortel, N V. ; VinÅ¡, V ; Watts, S ; Whitmore, J ; Wu, J: The TOTEM Experiment at the CERN Large Hadron Collider. In: *Journal of Instrumentation* 3 (2008), Nr. 08, S08007. http://stacks.iop.org/1748-0221/3/i=08/a=S08007

[38] Walenta, A.H. ; Fischer, J. ; Okuno, H. ; Wang, C.L.: Measurement of the Ionization Loss in the Region of Relativistic Rise for Noble and Molecular Gases. In: *Nucl.Instrum.Meth.* 161 (1979), S. 45–58. http://dx.doi.org/10.1016/0029-554X(79)90360-4. – DOI 10.1016/0029–554X(79)90360–4